Supplement of Atmos. Meas. Tech., 14, 4171–4185, 2021
https://doi.org/10.5194/amt-14-4171-2021-supplement

Atmospheric Measurement Techniques
Open Access
EGU

Supplement of

Detection of ship plumes from residual fuel operation in emission control areas using single-particle mass spectrometry

Johannes Passig et al.

Correspondence to: Johannes Passig (johannes.passig@uni-rostock.de)

Chemical signatures of main particle classes

The mass spectral signatures of all 300 inspected clusters as well as time series of their particle counts are provided in Figs. S5 and S6, the attribution to general classes is documented by Table S1.
Six general particle types were identified. Such groups have variations among their clusters, but similar signatures of the same overall chemical species as well as comparable temporal trends and size distributions. The labelling scheme reflects the most intense peaks and characteristic species for the respective general particle type and is frequently used in the literature (Ault et al., 2010; Decesari et al., 2014; Dall`Osto et al., 2016; Arndt et al., 2017). Their particle number and aerodynamic size can be found in Fig. S2(a), whereas average mass spectra of anions and cations are shown in Fig. S2(b) and (c), respectively. Carbon-containing particles contributed the majority to total particle numbers. Their spectra are either dominated by strong carbon cluster peaks from elemental carbon (EC), or by molecular fragments from organic carbon (OC). The balance between these signatures indicate the EC/OC ratio (Ferge et al., 2006; Spencer and Prather, 2006), however, in the present study this ratio is a continuum, broken into several small clusters by ART-2a (Zhou et al., 2006) and manually merged according to their dominant signals.
The EC-OC particle class shows no distinct K^+ peak, indicating fossil fuel combustion (oil burning or traffic) as most likely source. It has been shown that secondary material increases the particle's hygroscopicity (Moffet et al., 2008)(Ault et al., 2010; Decesari et al., 2014), suppressing the formation of negative ions (Neubauer et al., 1998; Hatch et al., 2014). The strong sulfate signal and the frequent absence of negative carbon clusters indicate condensation of sulfate during atmospheric transport, while its dominance over nitrate can result from processing in marine environment (Ault et al., 2010; Köllner et al., 2017), but also from the summer weather conditions due to the higher volatility of ammonium nitrate compared to ammonium sulfate (Querol et al., 2009; Arndt et al., 2017).
Particles with molecular fragment signals dominating over the carbon clusters were assigned to the OC-EC-nit class. They also show a pronounced K^+ peak and nitrogen-containing signals; both can be attributed to a higher contribution of biomass combustion (Silva et al., 1999; Pagels et al., 2013).
In the K-CN class, K^+ signals dominate the cation mass spectra, a well-documented signature for aerosols from biomass burning and wood combustion (Silva et al., 1999; Zhang et al., 2013). Potassium has a low ionization energy and the ion is energetically preferred compared to ions of other species, thus it survives collisions in the particle plume, when other ions are neutralized (Reinard and Johnston, 2008). The mass spectra of negative ions show CN^- and CNO^- signals from nitrogen-containing organic compounds (Silva et al., 1999; Köllner et al., 2017). A particle class similar to the K-CN particles, but with higher peaks from NO_2^- and NO_3^- indicate a strong contribution of secondary material, including nitrate in addition to the sulfate.
Sea salt particles are typically larger and produce characteristic signatures. Fresh sea salt particles are characterized by sodium ions (e.g. $^{23}Na^+$, $^{46}NaC^+$, $^{62}Na_2O^+$, $^{63}Na_2OH^+$), K^+, $^{16}O^-$ and $^{35,37}Cl^-$. (Dall'Osto et al., 2004; Murphy et al., 2019). Chlorine is replaced by nitrate during atmospheric processing (Gard et al., 1998), thus the strong nitrate signals and weak chlorine peaks ($^{35,37}Cl^-$) suggest that these particles are not fresh but have been transported over some distance.

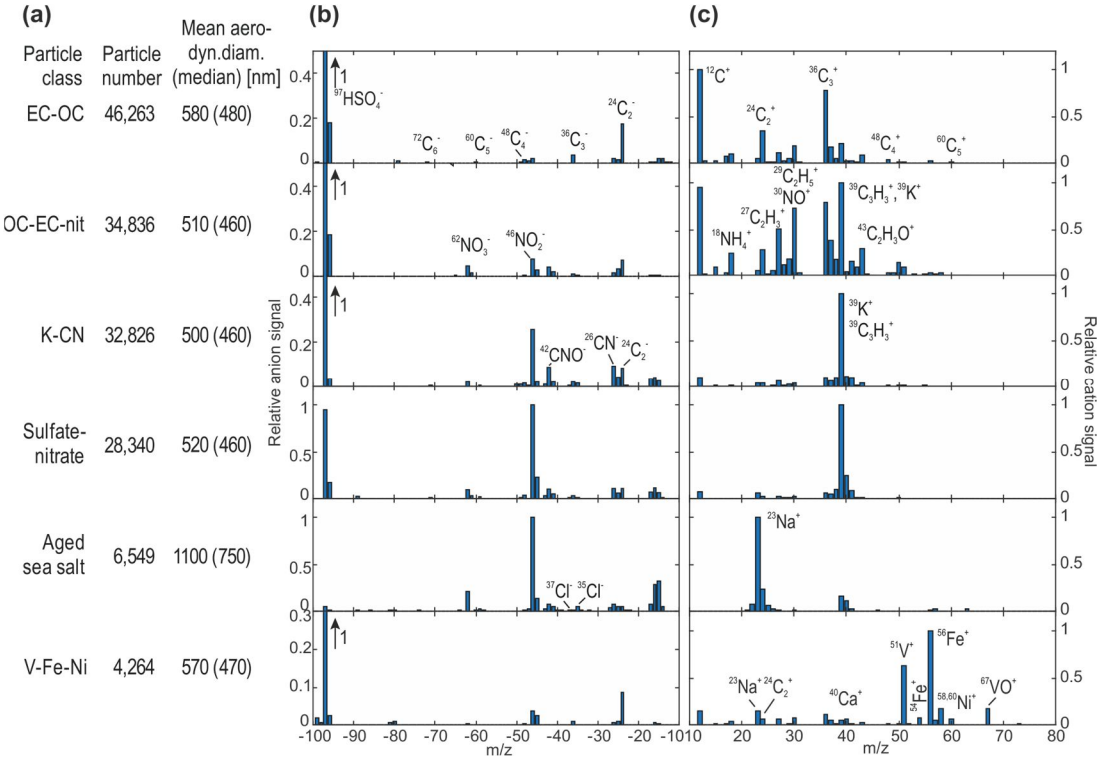

Figure S1: (a) General particle classes, their respective particle numbers and aerodynamic size. (b) Average anion mass spectra and (c) cation mass spectra of the particle classes. The mass spectra of the top 300 particle clusters from ART-2a analysis are shown in the Supplement and their assignment to the general classes is documented by Table S1.

Temporal signatures of main particle classes

Figure S2 (Fig. 3 in the manuscript) shows the time evolution of the six main particle classes with 10 minutes resolution.

The EC-OC particle numbers (dark grey area) exhibit a weak diurnal oscillation, however, not with enhanced levels during the morning and afternoon as expected from increased local traffic and human activity. In contrast, they follow the changes in wind direction and speed. It is conceivable that the northern winds transport local emissions from the city center to the sampling site, however, the strong sulfate peaks in the EC-OC group and the lack of negative ions point on aged particles that might have been transported over larger distances, see Fig. S1. Also the particle size is larger than typical for urban traffic emissions (Dall`Osto et al., 2016) which is in agreement with the assumption that these freshly emitted particles are underrepresented compared to the larger ones that are enriched by the aerosol concentrator.

The OC-EC-nit, K-Cn and Sulfate-nitrate particles roughly follow the trend of the EC-OC particles, but show an additional diurnal variation that is especially pronounced during the last two days of the measurements. Their particle numbers increase after sunset and drop in the morning, reflecting condensation of semi-volatile components at night. This temporal behavior is comparable for OC-EC-nit, K-CN and Sulfate-Nitrate particles, because: (I) They are all composed of organic matter to some extend. (II) They can simultaneously grow into the efficiently detected size mode by condensation of secondary material, and (III) all possible diurnal features of aerosol chemistry, such as daytime photochemical formation of SOA or increases in nitrate with relative humidity (Salcedo et al., 2006; Dall'Osto et al., 2009; Healy et al., 2012) are interfered by the strong land/onshore circulation. This dominance of air circulation over local atmospheric chemistry is also reflected by the pronounced particle number maxima during the last nights of the measurement period, where local terrestrial air masses contribute. In contrast, during the second and third night, the air trajectories passed over less land before entering the site and the maxima are substantially smaller. Also the OC-EC-nit and K-CN particle numbers follow the diurnal trend, probably because they grow by night-time condensation into the size mode that is enriched by the aerosol concentrator, while local emissions of smaller particles are barely detected. However, a small transient feature of K-CN particles can be noticed at the 29th June at 8 pm, before the general increase after sunset around 10 pm. It might be associated with local emissions, e.g. from barbecuing. The enhanced contributions of aged sea salt at the 30th June can be attributed to stronger winds in the central Baltic Sea.

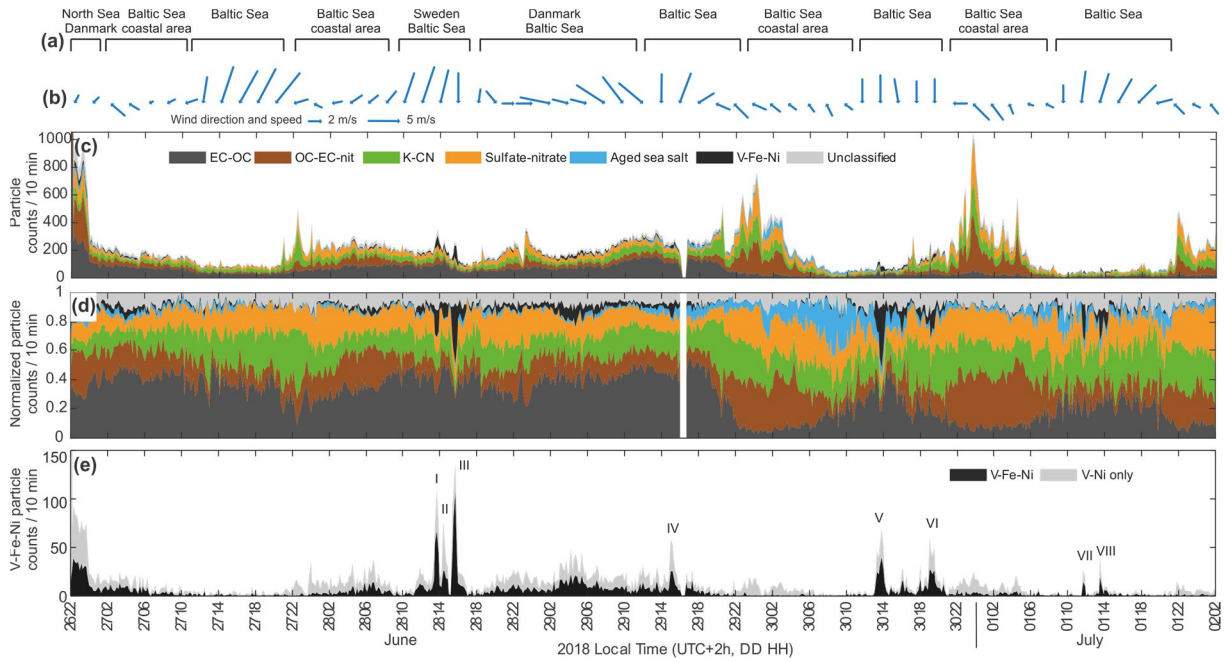

Figure S2 (Fig. 3 in the manuscript): (a) Air mass origin (top row: >12 h, bottom row <12 h) according to the HYSPLIT back trajectory analysis (Fig. S2 and S3). (b) Measured wind data from the meteorological station at the harbor exit, 12 km north of the measurement site. (c) The time series of particle counts from the general particle classes shows regional/long-range transported air pollution (26-29 June) and night-time secondary organic aerosol formation (29 June – 02 July). (d) The same data as (c), but normalized to total particle counts illustrate the contribution of each particle type as well as increased sea-salt levels during the 30 June. (e) The temporal behavior of V-Fe-Ni particles from residual fuel combustion reveals transient events and smooth background signals, predominantly during onshore winds. Apart from the short events, their contribution to total particle numbers is low.

Experiments on the research ship engine

To provide an estimate of the Fe resonance effect on particle detection in a ship plume, we conducted on-line experiments using a one-cylinder four-stroke, common rail injection diesel research ship engine with 75 kW maximum power, installed at the "Institute of Piston Machines and Internal Combustion Engines", University of Rostock, Germany (Streibel et al., 2017). Aerosols were sampled from the hot flue gas and mixed into a stream of 5 m^3/min outdoor ambient air in a home-build dilution tunnel of 3 m length and 15 cm diameter. 1 l/min of the diluted and cooled aerosol was guided to the SPMS instrument. We compared our KrF-excimer laser at 248 nm inducing the Fe resonance with the most common laser system in SPMS, the Nd:YAG at 266 nm, both operated with a pulse duration of about 5 ns, the same pulse energy of 1.6 mJ. The focal lens (f=200 mm) was adjusted to maintain a comparable spot area, respective intensity for both wavelengths.

Key idea to mimic ambient aerosols containing contributions from ships after atmospheric transport is the use of diesel fuel during measurements and previous engine operation with bunker fuel to generate particles with small impurities from bunker fuel by carryover effects.

The on-line experiments were conducted at 75 kW (100%) load after a sufficient warm-up time and a 30 min run-in period at full load. Measurements with the Nd:YAG laser were performed 15 total operation hours after switching to diesel fuel, in which the engine consumed 65 kg diesel fuel for an energy output of 225 kWh. For the KrF-excimer laser, the experiment was repeated on the next day without switching back to bunker oil. At this time, the engine was run for 22 hours on diesel, with a total fuel consumption of 123 kg and 441 kWh energy output since switching from bunker oil to diesel.

A single-particle investigation reveals that many more particles show clear signatures of the residuals V, Ni, and Fe if ionized with 248 nm, despite the longer engine operation time (22h for 248 nm vs. 15h for 266 nm) since switching from bunker fuel to diesel (Fig. S3). One explanation for the increased detection efficiency for V and Ni lies in the complex UV absorption spectra of these metals, with possibly more and stronger lines overlapping with the rather broad KrF laser spectrum compared to the Nd:YAG laser (Passig et al., 2020) .

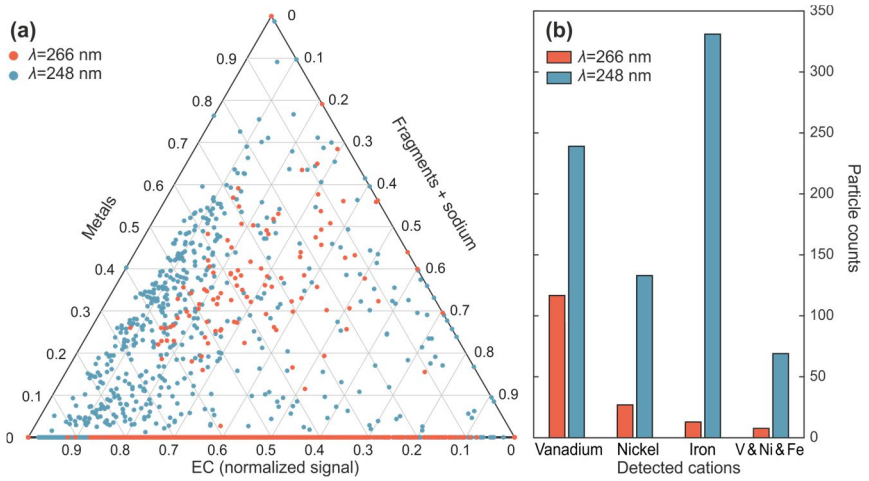

Fig. S3 Metal residues from previous bunker fuel use in ship engine particles, emitted during diesel fuel operation. (A) Ternary plot of single particle composition (each 2000 particles) indicates a minor particle fraction with high metal content (predominantly V^+) for ionization with 266 nm (red dots). Ionization with 248 nm reveals metal signatures for many more particles, also with lower concentrations (blue dots). Particles without metal signals result in dots at the bottom line. (EC signal: sum of C_3^+, C_4^+, C_5^+; fragments/sodium: sum of C^+, Na^+, $C_3H_3O^+$, $C_3H_7^+$; metals: 3x sum of V^+, VO^+, $^{54}Fe^+$,$^{58}Ni^+$). (B) From each 2000 particles, many more show clear metal signatures if ionized with 248 nm. The largest difference can be noticed for iron, a consequence of direct resonance. To reduce ambiguity, particles are counted to the respective group only if the following signals are above noise level: both V^+ and VO^+ for V, $^{54}Fe^+$ and $^{56}Fe^+$ for Fe, $^{58}Ni^+$ for Ni.

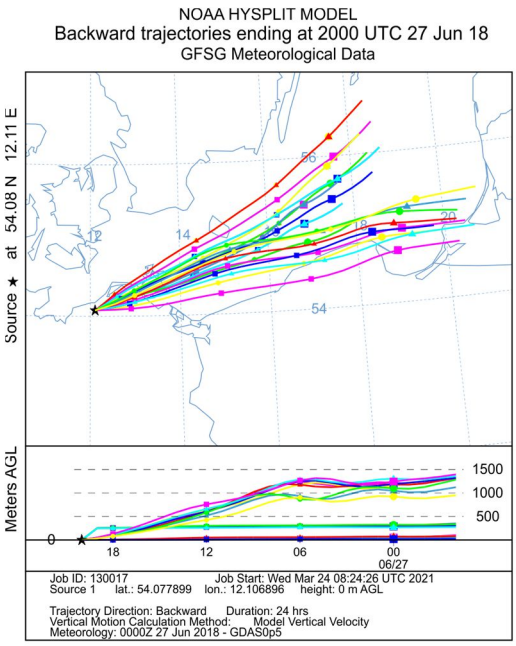

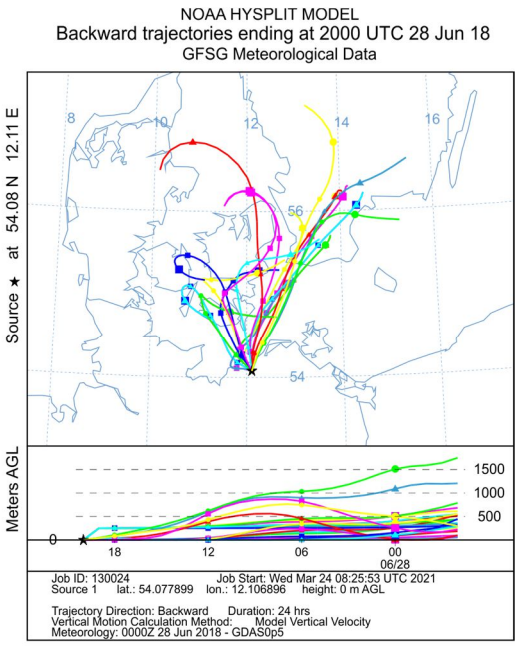

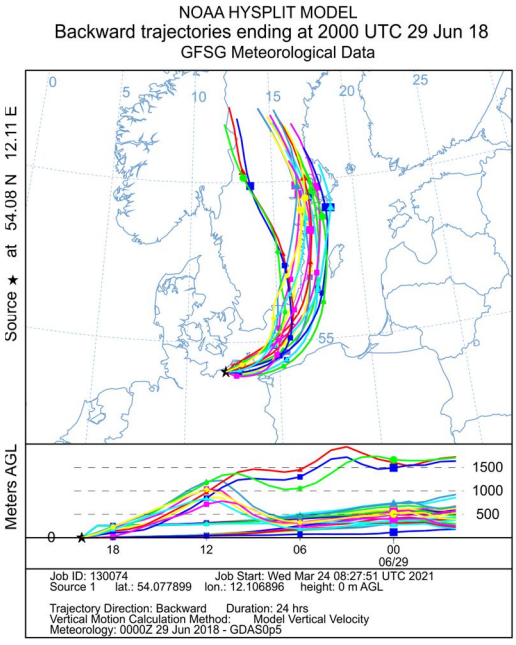

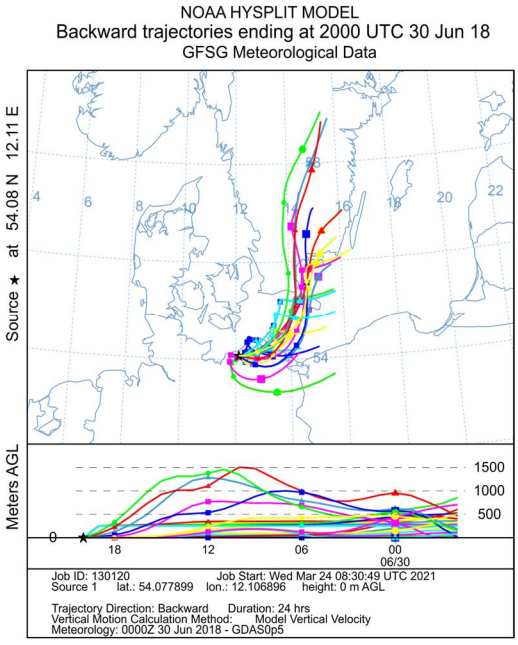

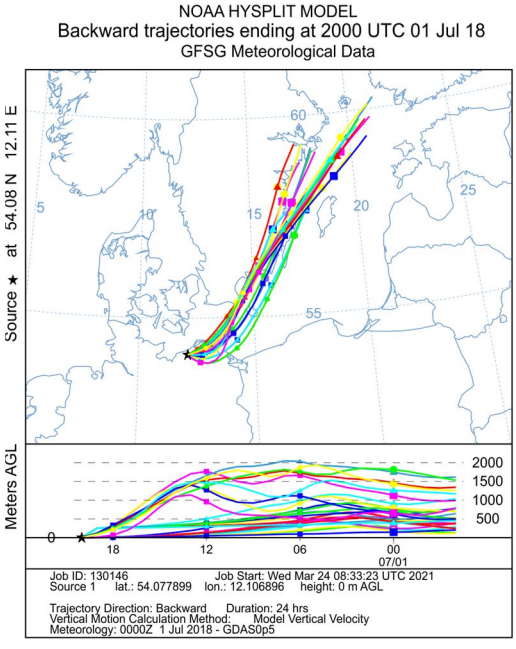

Figure S4: HYSPLIT back trajectories for 24h run time, ending at the measurement site during the experiments.

Table S1: Assignment of the top-300 clusters of the ART-2a analysis to main particle classes.

EC-OC	OC-EC-nit	Sulfate-nitrate	K-CN		aged sea salt	V-Fe-Ni	other	remarks
3	1	24	2		57	72		
5	7	30	4		80	97	43	NO+
8	14	31	6		82	110	44	NO+
10	18	32	9		106	111	45	NO+
11	20	39	12		120	127	89	Al+ Fe+ org
13	26	41	21		132	138	152	low quality
15	27	51	23		146	150	174	Ca+, large
16	28	52	34		155	151	184	Al+ org.
17	33	62	35		159	161	206	Fe+43
19	40	64	42	local	177	164	212	EC-S
22	43	69	47		180	183	222	MGO?
25	44	70	49		193	196	236	Fe+ Ni+
29	45	73	51		225	226	256	low quality
36	53	75	56		234	230	287	Fe+
37	54	95	65	local	246	250	296	Fe+
38	59	96	67	local	252	265		
44	66	100	84		253			
46	68	101	86		254			
48	74	104	90		257			
50	77	105	83		259			
55	78	112	85		260			
58	87	115	91		266			
60	88	117	92		267			
63	102	121	98		287			
71	107	124	114					
76	109	126	118					
79	113	128	122					
81	116	130	125					
93	123	131	129					
94	135	136	133					
99	139	137	140					
103	141	143	149					
108	182	147	153					
119	187	148	154					
134	199	156	157					
142	200	158	192					
144	205	160	210					
145	215	162	211					
163	216	165	213					
170	219	166	224					
171	223	167	235					
178	228	168	261					
185	229	169	282					
186	231	172	281					
190	232	173						
194	236	175						
201	238	176						
202	242	179						
204	243	181						
207	244	188						
208	247	189						
214	249	191						
218	251	195						
221	258	197						
222	264	198						
227	268	203						
233	275	209						
239	279	217						
245	283	220						
248	284	240						
255	280	241						
262	286	263						
269	289	270						
273	290	272						
276	292	274						
277	293	291						
278	297	295						
285								

283
284
288
294
298
299
300

References

Arndt, J., Sciare, J., Mallet, M., Roberts, G. C., Marchand, N., Sartelet, K., Sellegri, K., Dulac, F., Healy, R. M., and Wenger, J. C.: Sources and mixing state of summertime background aerosol in the north-western Mediterranean basin, Atmos. Chem. Phys., 17, 6975–7001, https://doi.org/10.5194/acp-17-6975-2017, 2017.

Ault, A. P., Gaston, C. I., Wang, Y., Dominguez, G., Thiemens, M. H., and Prather, K. A.: Characterization of the single particle mixing state of individual ship plume events measured at the Port of Los Angeles, Environ. Sci. Technol., 44, 1954–1961, https://doi.org/10.1021/es902985h, 2010.

Dall`Osto, M., Beddows, D. C. S., McGillicuddy, E. J., Esser-Gietl, J. K., Harrison, R. M., and Wenger, J. C.: On the simultaneous deployment of two single-particle mass spectrometers at an urban background and a roadside site during SAPUSS, Atmos. Chem. Phys., 16, 9693–9710, https://doi.org/10.5194/acp-16-9693-2016, 2016.

Dall'Osto, M., Harrison, R. M., Coe, H., Williams, P. I., and Allan, J. D.: Real time chemical characterization of local and regional nitrate aerosols, Atmos. Chem. Phys., 9, 3709–3720, https://doi.org/10.5194/acp-9-3709-2009, 2009.

Dall'Osto, M., Beddows, D. C. S., Kinnersley, R. P., Harrison, R. M., Donovan, R. J., and Heal, M. R.: Characterization of individual airborne particles by using aerosol time-of-flight mass spectrometry at Mace Head, Ireland, J. Geophys. Res., 109, https://doi.org/10.1029/2004JD004747, 2004.

Decesari, S., Allan, J., Plass-Duelmer, C., Williams, B. J., Paglione, M., Facchini, M. C., O'Dowd, C., Harrison, R. M., Gietl, J. K., Coe, H., Giulianelli, L., Gobbi, G. P., Lanconelli, C., Carbone, C., Worsnop, D., Lambe, A. T., Ahern, A. T., Moretti, F., Tagliavini, E., Elste, T., Gilge, S., Zhang, Y., and Dall'Osto, M.: Measurements of the aerosol chemical composition and mixing state in the Po Valley using multiple spectroscopic techniques, Atmos. Chem. Phys., 14, 12109–12132, https://doi.org/10.5194/acp-14-12109-2014, 2014.

Ferge, T., Karg, E., Schröppel, A., Coffee, K. R., Tobias, H. J., Frank, M., Gard, E. E., and Zimmermann, R.: Fast determination of the relative elemental and organic carbon content of aerosol samples by on-line single-particle aerosol time-of-flight mass spectrometry, Environ. Sci. Technol., 40, 3327–3335, https://doi.org/10.1021/es050799k, 2006.

Gard, Kleeman, Gross, Hughes, Allen, Morrical, Fergenson, Dienes, E, G. M., Johnson, Cass, and Prather: Direct observation of heterogeneous chemistry in the atmosphere, Science, 279, 1184–1187, https://doi.org/10.1126/science.279.5354.1184, 1998.

Hatch, L. E., Pratt, K. A., Huffman, J. A., Jimenez, J. L., and Prather, K. A.: Impacts of Aerosol Aging on Laser Desorption/Ionization in Single-Particle Mass Spectrometers, Aerosol Sci. Technol., 48, 1050–1058, https://doi.org/10.1080/02786826.2014.955907, 2014.

Healy, R. M., Sciare, J., Poulain, L., Kamili, K., Merkel, M., Müller, T., Wiedensohler, A., Eckhardt, S., Stohl, A., Sarda-Estève, R., McGillicuddy, E., O'Connor, I. P., Sodeau, J. R., and Wenger, J. C.: Sources and mixing state of size-resolved elemental carbon particles in a European megacity: Paris, Atmos. Chem. Phys., 12, 1681–1700, https://doi.org/10.5194/acp-12-1681-2012, 2012.

Köllner, F., Schneider, J., Willis, M. D., Klimach, T., Helleis, F., Bozem, H., Kunkel, D., Hoor, P., Burkart, J., Leaitch, W. R., Aliabadi, A. A., Abbatt, J. P. D., Herber, A. B., and Borrmann, S.: Particulate trimethylamine in the summertime Canadian high Arctic lower troposphere, Atmos. Chem. Phys., 17, 13747–13766, https://doi.org/10.5194/acp-17-13747-2017, 2017.

Moffet, R. C., Qin, X., Rebotier, T., Furutani, H., and Prather, K. A.: Chemically segregated optical and microphysical properties of ambient aerosols measured in a single-particle mass spectrometer, J. Geophys. Res., 113, https://doi.org/10.1029/2007JD009393, 2008.

Murphy, D. M., Froyd, K. D., Bian, H., Brock, C. A., Dibb, J. E., DiGangi, J. P., Diskin, G., Dollner, M., Kupc, A., Scheuer, E. M., Schill, G. P., Weinzierl, B., Williamson, C. J., and Yu, P.: The distribution of sea-salt aerosol in the global troposphere, Atmos. Chem. Phys., 19, 4093–4104, https://doi.org/10.5194/acp-19-4093-2019, 2019.

Neubauer, K. R., Johnston, M. V., and Wexler, A. S.: Humidity effects on the mass spectra of single aerosol particles, Atmos. Environ., 32, 2521–2529, https://doi.org/10.1016/S1352-2310(98)00005-3, 1998.

Pagels, J., Dutcher, D. D., Stolzenburg, M. R., McMurry, P. H., Gälli, M. E., and Gross, D. S.: Fine-particle emissions from solid biofuel combustion studied with single-particle mass spectrometry: Identification of

markers for organics, soot, and ash components, J. Geophys. Res., 118, 859–870, https://doi.org/10.1029/2012JD018389, 2013.
Passig, J., Schade, J., Rosewig, E. I., Irsig, R., Kröger-Badge, T., Czech, H., Sklorz, M., Streibel, T., Li, L., Li, X., Zhou, Z., Fallgren, H., Moldanova, J., and Zimmermann, R.: Resonance-enhanced detection of metals in aerosols using single-particle mass spectrometry, Atmos. Chem. Phys., 20, 7139–7152, https://doi.org/10.5194/acp-20-7139-2020, 2020.
Querol, X., Alastuey, A., Pey, J., Cusack, M., Pérez, N., Mihalopoulos, N., Theodosi, C., Gerasopoulos, E., Kubilay, N., and Koçak, M.: Variability in regional background aerosols within the Mediterranean, Atmos. Chem. Phys., 9, 4575–4591, https://doi.org/10.5194/acp-9-4575-2009, 2009.
Reinard, M. S. and Johnston, M. V.: Ion formation mechanism in laser desorption ionization of individual nanoparticles, J. Am. Soc. Spectrom., 19, 389–399, https://doi.org/10.1016/j.jasms.2007.11.017, 2008.
Salcedo, D., Onasch, T. B., Dzepina, K., Canagaratna, M. R., Zhang, Q., Huffman, J. A., DeCarlo, P. F., Jayne, J. T., Mortimer, P., Worsnop, D. R., Kolb, C. E., Johnson, K. S., Zuberi, B., Marr, L. C., Volkamer, R., Molina, L. T., Molina, M. J., Cardenas, B., Bernabé, R. M., Márquez, C., Gaffney, J. S., Marley, N. A., Laskin, A., Shutthanandan, V., Xie, Y., Brune, W., Lesher, R., Shirley, T., and Jimenez, J. L.: Characterization of ambient aerosols in Mexico City during the MCMA-2003 campaign with Aerosol Mass Spectrometry: results from the CENICA Supersite, Atmos. Chem. Phys., 6, 925–946, https://doi.org/10.5194/acp-6-925-2006, 2006.
Silva, P. J., Liu, D.-Y., Noble, C. A., and Prather, K. A.: Size and Chemical Characterization of Individual Particles Resulting from Biomass Burning of Local Southern California Species, Environ. Sci. Technol., 33, 3068–3076, https://doi.org/10.1021/es980544p, 1999.
Spencer, M. T. and Prather, K. A.: Using ATOFMS to Determine OC/EC Mass Fractions in Particles, Aerosol Sci. Technol., 40, 585–594, https://doi.org/10.1080/02786820600729138, 2006.
Streibel, T., Schnelle-Kreis, J., Czech, H., Harndorf, H., Jakobi, G., Jokiniemi, J., Karg, E., Lintelmann, J., Matuschek, G., Michalke, B., Müller, L., Orasche, J., Passig, J., Radischat, C., Rabe, R., Reda, A., Rüger, C., Schwemer, T., Sippula, O., Stengel, B., Sklorz, M., Torvela, T., Weggler, B., and Zimmermann, R.: Aerosol emissions of a ship diesel engine operated with diesel fuel or heavy fuel oil, Environ. Sci. Pollut. Res. Int., 24, 10976–10991, https://doi.org/10.1007/s11356-016-6724-z, 2017.
Zhang, G., Bi, X., Li, L., Chan, L. Y., Li, M., Wang, X., Sheng, G., Fu, J., and Zhou, Z.: Mixing state of individual submicron carbon-containing particles during spring and fall seasons in urban Guangzhou, China: a case study, Atmos. Chem. Phys., 13, 4723–4735, https://doi.org/10.5194/acp-13-4723-2013, 2013.
Zhou, L., Hopke, P. K., and Venkatachari, P.: Cluster analysis of single particle mass spectra measured at Flushing, NY, Anal. Chim. Acta, 555, 47–56, https://doi.org/10.1016/j.aca.2005.08.061, 2006.

Figure S4: Weight matrices (neg. and pos. mass spectra) of the top 300 cluster centers from the ART-2a analysis.

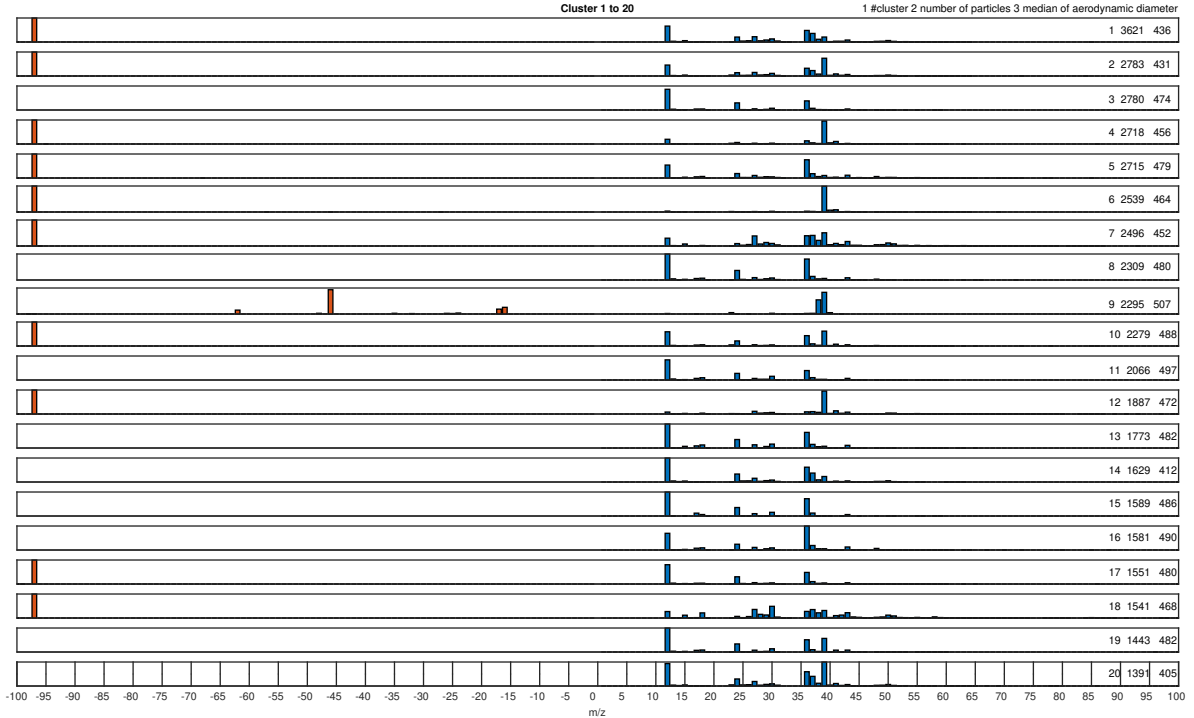

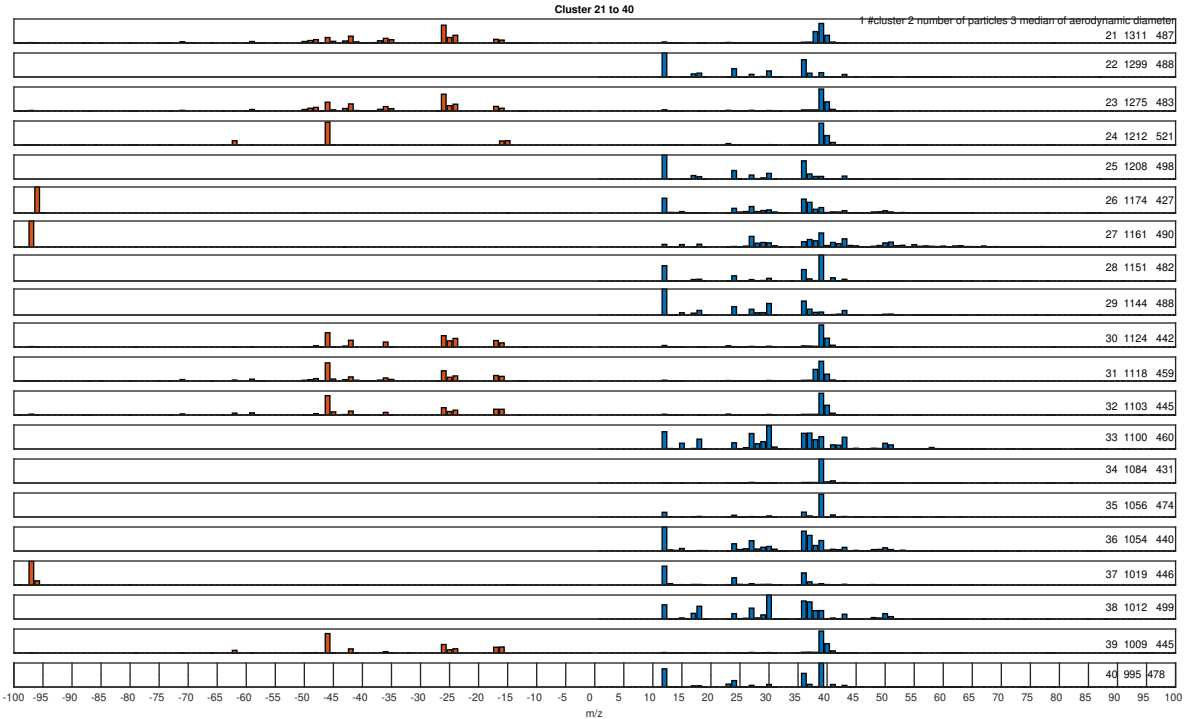
Cluster 21 to 40
1 #cluster 2 number of particles 3 median of aerodynamic diameter
21 1311 487
22 1299 488
23 1275 483
24 1212 521
25 1208 498
26 1174 427
27 1161 490
28 1151 482
29 1144 488
30 1124 442
31 1118 459
32 1103 445
33 1100 460
34 1084 431
35 1056 474
36 1054 440
37 1019 446
38 1012 499
39 1009 445
40 995 478
-100 -95 -90 -85 -80 -75 -70 -65 -60 -55 -50 -45 -40 -35 -30 -25 -20 -15 -10 -5 0 5 10 15 20 25 30 35 40 45 50 55 60 65 70 75 80 85 90 95 100
m/z

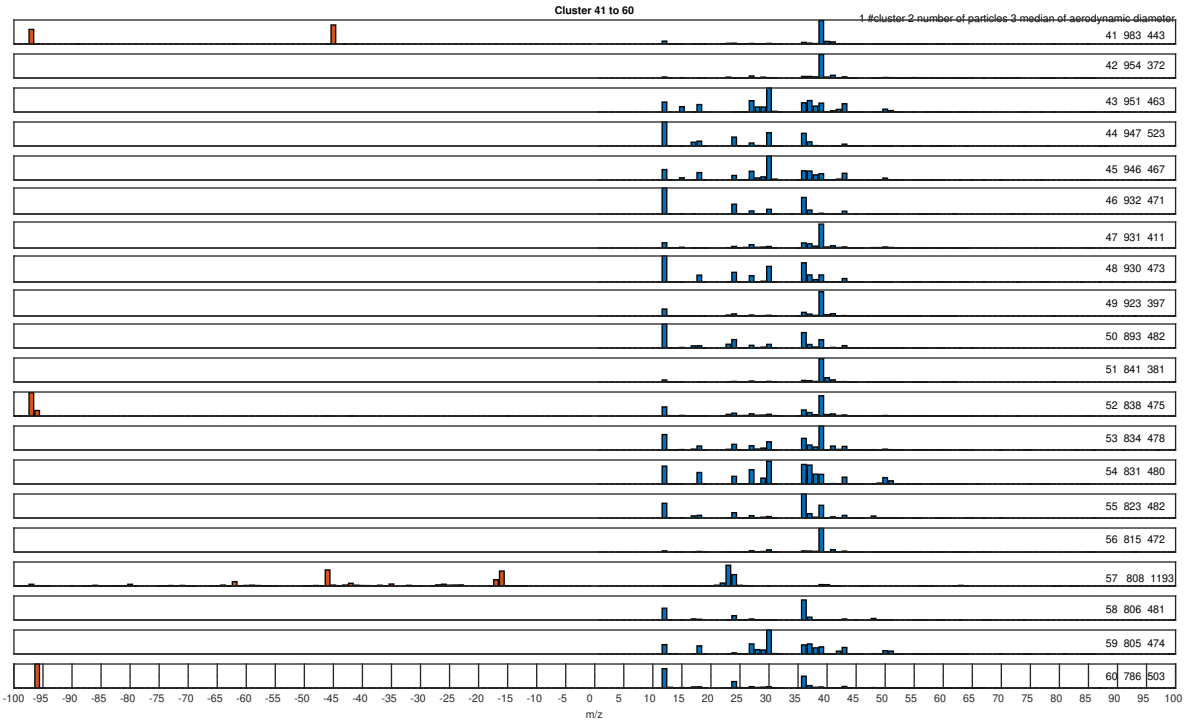
Cluster 41 to 60
1 #cluster 2 number of particles 3 median of aerodynamic diameter
41 983 443
42 954 372
43 951 463
44 947 523
45 946 467
46 932 471
47 931 411
48 930 473
49 923 397
50 893 482
51 841 381
52 838 475
53 834 478
54 831 480
55 823 482
56 815 472
57 808 1193
58 806 481
59 805 474
60 786 503
-100 -95 -90 -85 -80 -75 -70 -65 -60 -55 -50 -45 -40 -35 -30 -25 -20 -15 -10 -5 0 5 10 15 20 25 30 35 40 45 50 55 60 65 70 75 80 85 90 95 100
m/z

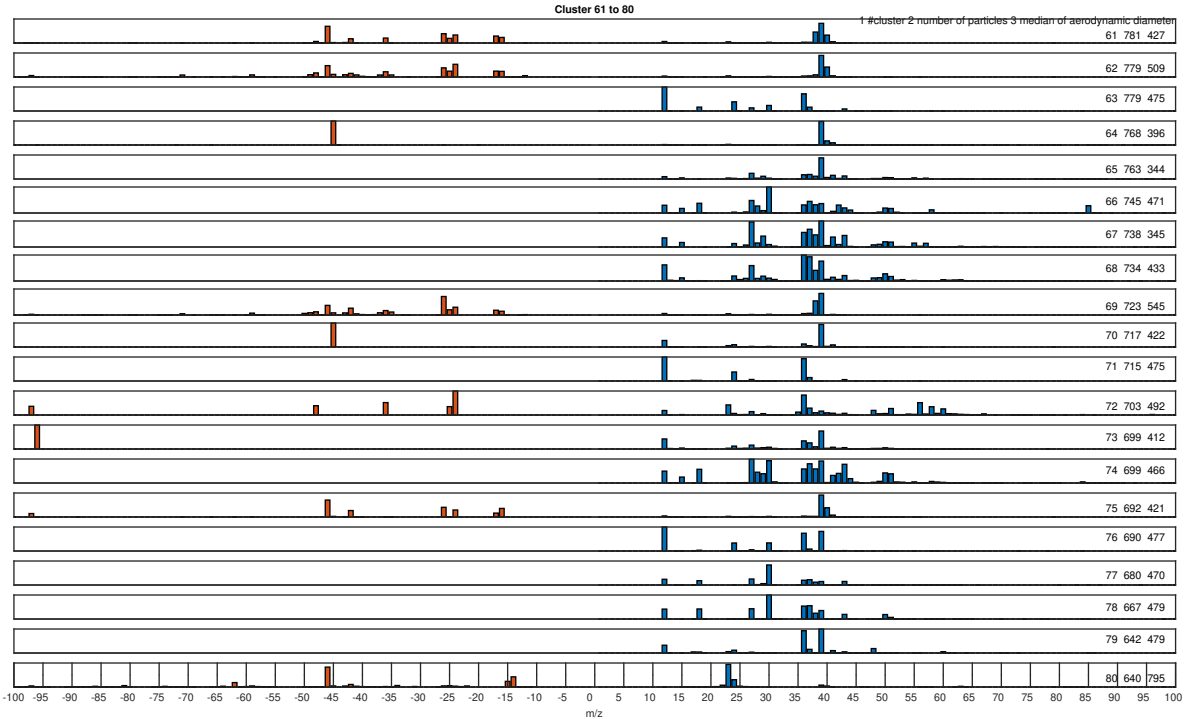
Cluster 61 to 80
1 #cluster 2 number of particles 3 median of aerodynamic diameter
61 781 427
62 779 509
63 779 475
64 768 396
65 763 344
66 745 471
67 738 345
68 734 433
69 723 545
70 717 422
71 715 475
72 703 492
73 699 412
74 699 466
75 692 421
76 690 477
77 680 470
78 667 479
79 642 479
80 640 795
-100 -95 -90 -85 -80 -75 -70 -65 -60 -55 -50 -45 -40 -35 -30 -25 -20 -15 -10 -5 0 5 10 15 20 25 30 35 40 45 50 55 60 65 70 75 80 85 90 95 100
m/z

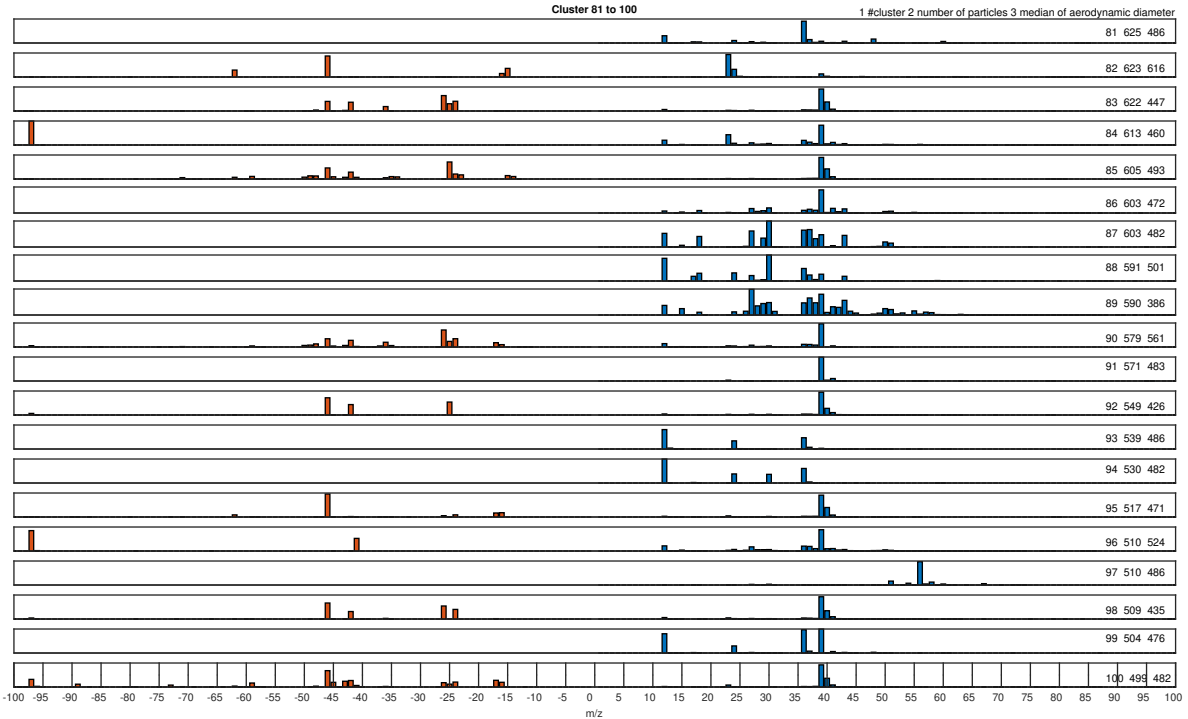
Cluster 81 to 100
1 #cluster 2 number of particles 3 median of aerodynamic diameter
81 625 486
82 623 616
83 622 447
84 613 460
85 605 493
86 603 472
87 603 482
88 591 501
89 590 386
90 579 561
91 571 483
92 549 426
93 539 486
94 530 482
95 517 471
96 510 524
97 510 486
98 509 435
99 504 476
100 499 482
-100 -95 -90 -85 -80 -75 -70 -65 -60 -55 -50 -45 -40 -35 -30 -25 -20 -15 -10 -5 0 5 10 15 20 25 30 35 40 45 50 55 60 65 70 75 80 85 90 95 100
m/z

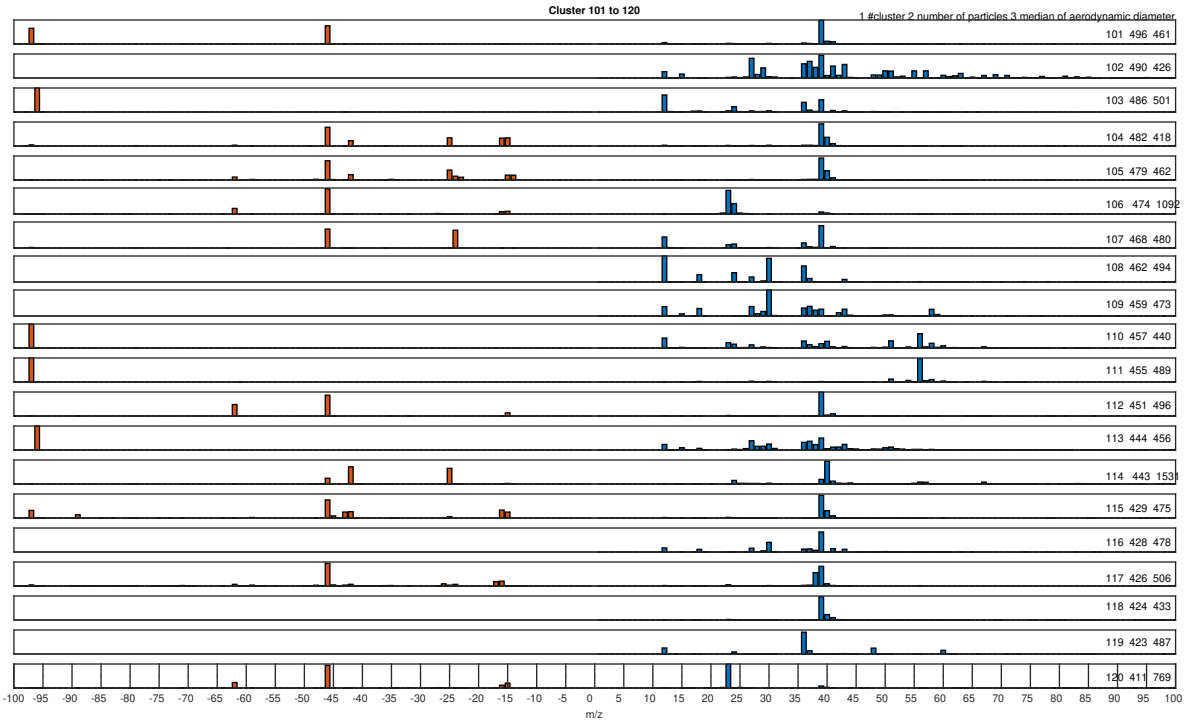
Cluster 101 to 120
1 #cluster 2 number of particles 3 median of aerodynamic diameter
101 496 461
102 490 426
103 486 501
104 482 418
105 479 462
106 474 1092
107 468 480
108 462 494
109 459 473
110 457 440
111 455 489
112 451 496
113 444 456
114 443 1531
115 429 475
116 428 478
117 426 506
118 424 433
119 423 487
120 411 769
-100 -95 -90 -85 -80 -75 -70 -65 -60 -55 -50 -45 -40 -35 -30 -25 -20 -15 -10 -5 0 5 10 15 20 25 30 35 40 45 50 55 60 65 70 75 80 85 90 95 100
m/z

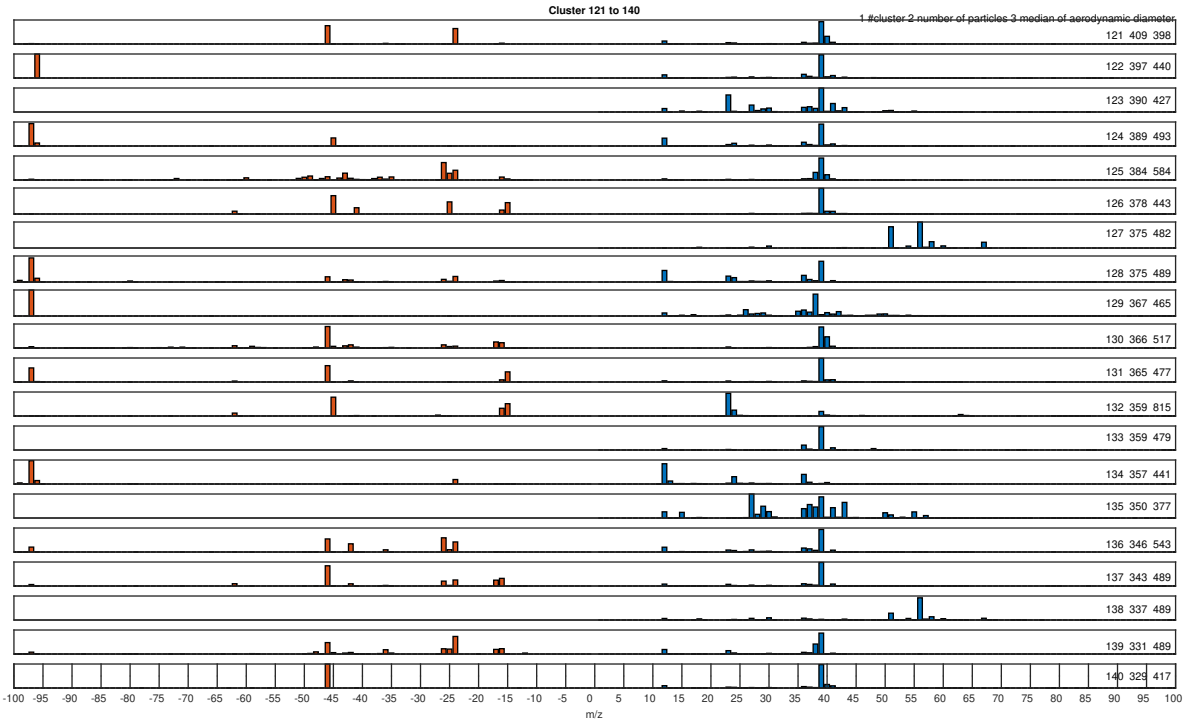
Cluster 121 to 140
1 #cluster 2 number of particles 3 median of aerodynamic diameter
121 409 398
122 397 440
123 390 427
124 389 493
125 384 584
126 378 443
127 375 482
128 375 489
129 367 465
130 366 517
131 365 477
132 359 815
133 359 479
134 357 441
135 350 377
136 346 543
137 343 489
138 337 489
139 331 489
140 329 417
-100 -95 -90 -85 -80 -75 -70 -65 -60 -55 -50 -45 -40 -35 -30 -25 -20 -15 -10 -5 0 5 10 15 20 25 30 35 40 45 50 55 60 65 70 75 80 85 90 95 100
m/z

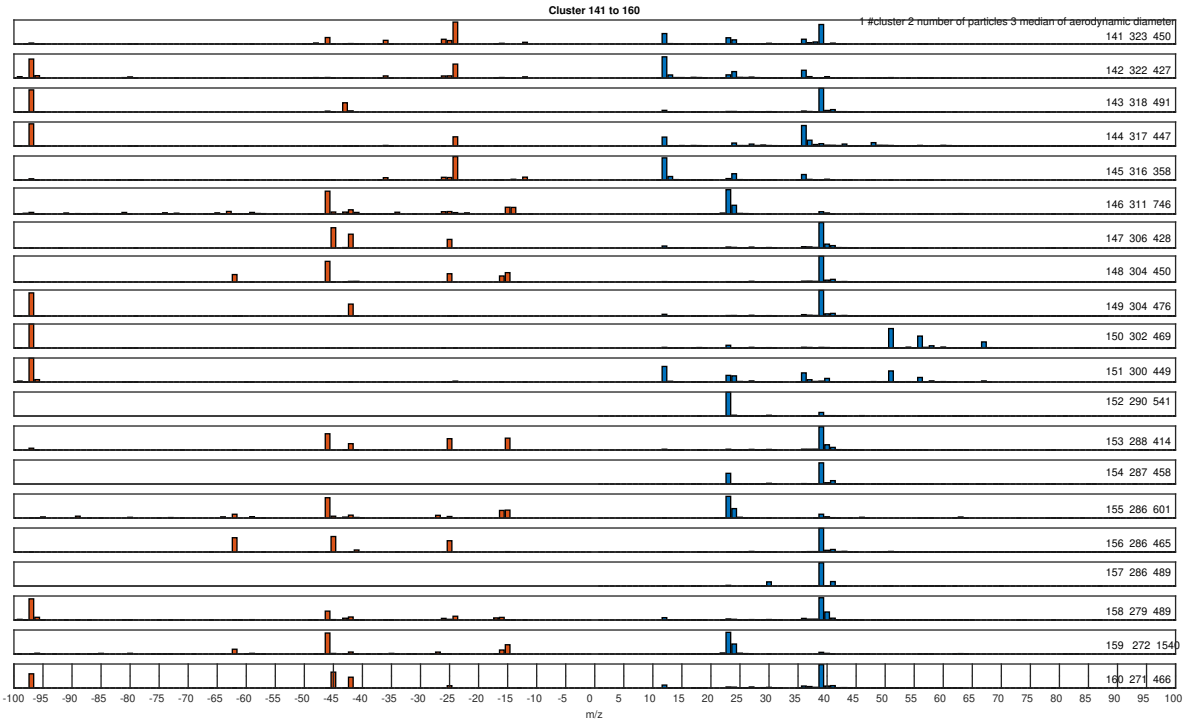
Cluster 141 to 160
1 #cluster 2 number of particles 3 median of aerodynamic diameter
141 323 450
142 322 427
143 318 491
144 317 447
145 316 358
146 311 746
147 306 428
148 304 450
149 304 476
150 302 469
151 300 449
152 290 541
153 288 414
154 287 458
155 286 601
156 286 465
157 286 489
158 279 489
159 272 1540
160 271 466
-100 -95 -90 -85 -80 -75 -70 -65 -60 -55 -50 -45 -40 -35 -30 -25 -20 -15 -10 -5 0 5 10 15 20 25 30 35 40 45 50 55 60 65 70 75 80 85 90 95 100
m/z

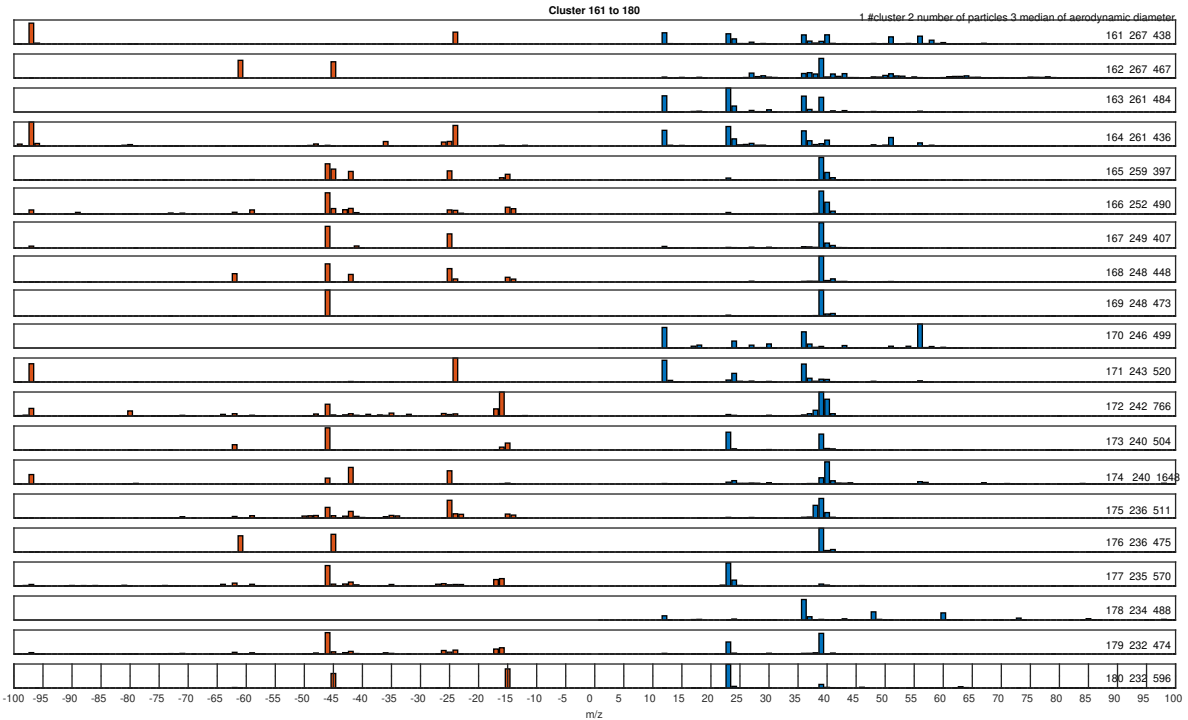
Cluster 161 to 180
1 #cluster 2 number of particles 3 median of aerodynamic diameter
161 267 438
162 267 467
163 261 484
164 261 436
165 259 397
166 252 490
167 249 407
168 248 448
169 248 473
170 246 499
171 243 520
172 242 766
173 240 504
174 240 1648
175 236 511
176 236 475
177 235 570
178 234 488
179 232 474
180 232 596
-100 -95 -90 -85 -80 -75 -70 -65 -60 -55 -50 -45 -40 -35 -30 -25 -20 -15 -10 -5 0 5 10 15 20 25 30 35 40 45 50 55 60 65 70 75 80 85 90 95 100
m/z

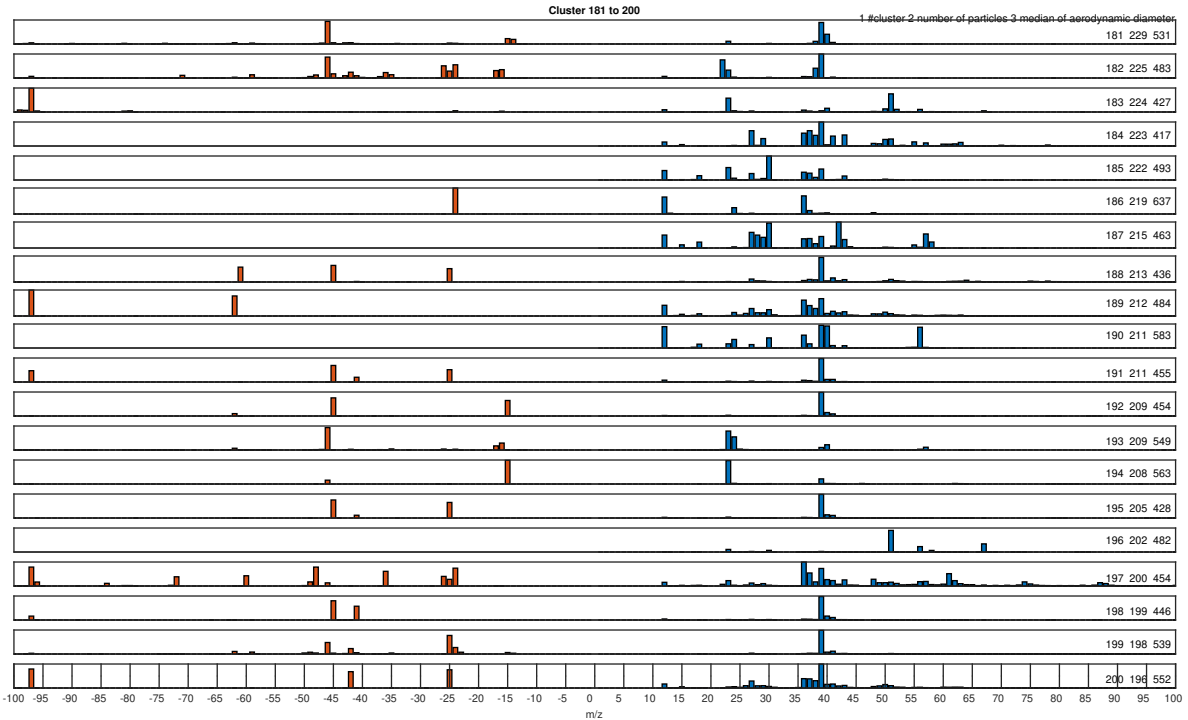
Cluster 181 to 200
1 #cluster 2 number of particles 3 median of aerodynamic diameter
181 229 531
182 225 483
183 224 427
184 223 417
185 222 493
186 219 637
187 215 463
188 213 436
189 212 484
190 211 583
191 211 455
192 209 454
193 209 549
194 208 563
195 205 428
196 202 482
197 200 454
198 199 446
199 198 539
200 196 552
-100 -95 -90 -85 -80 -75 -70 -65 -60 -55 -50 -45 -40 -35 -30 -25 -20 -15 -10 -5 0 5 10 15 20 25 30 35 40 45 50 55 60 65 70 75 80 85 90 95 100
m/z

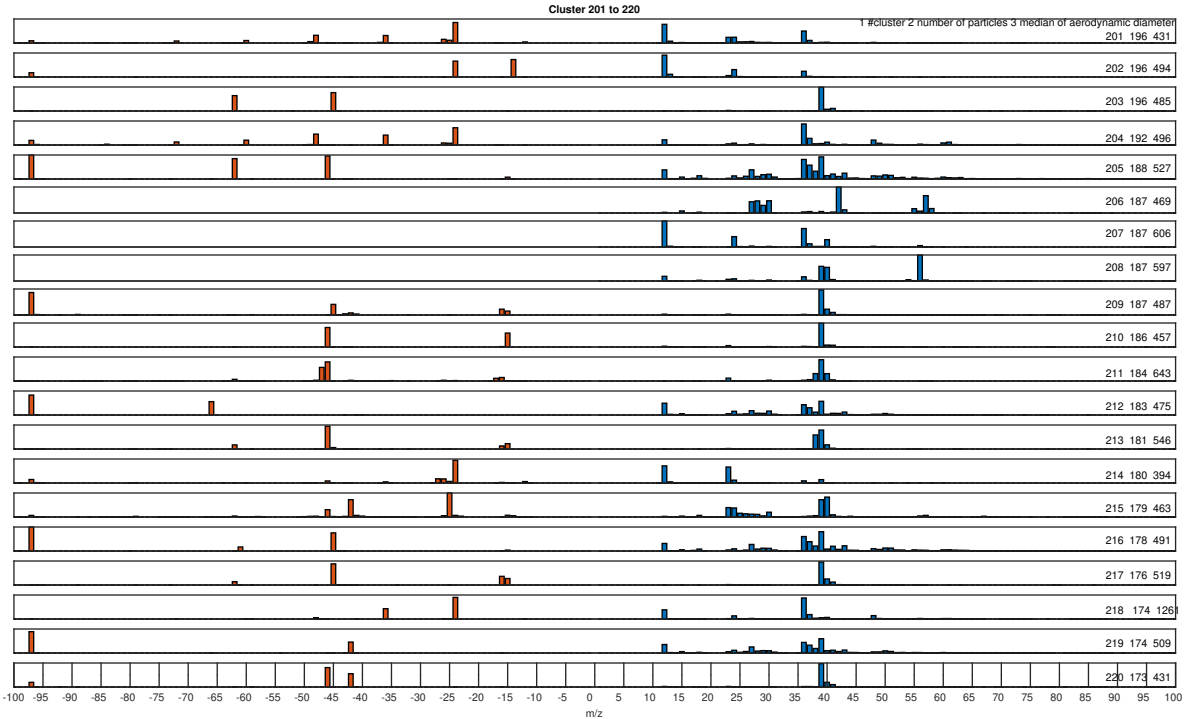
Cluster 201 to 220
1 #cluster 2 number of particles 3 median of aerodynamic diameter
201 196 431
202 196 494
203 196 485
204 192 496
205 188 527
206 187 469
207 187 606
208 187 597
209 187 487
210 186 457
211 184 643
212 183 475
213 181 546
214 180 394
215 179 463
216 178 491
217 176 519
218 174 1261
219 174 509
220 173 431
-100 -95 -90 -85 -80 -75 -70 -65 -60 -55 -50 -45 -40 -35 -30 -25 -20 -15 -10 -5 0 5 10 15 20 25 30 35 40 45 50 55 60 65 70 75 80 85 90 95 100
m/z

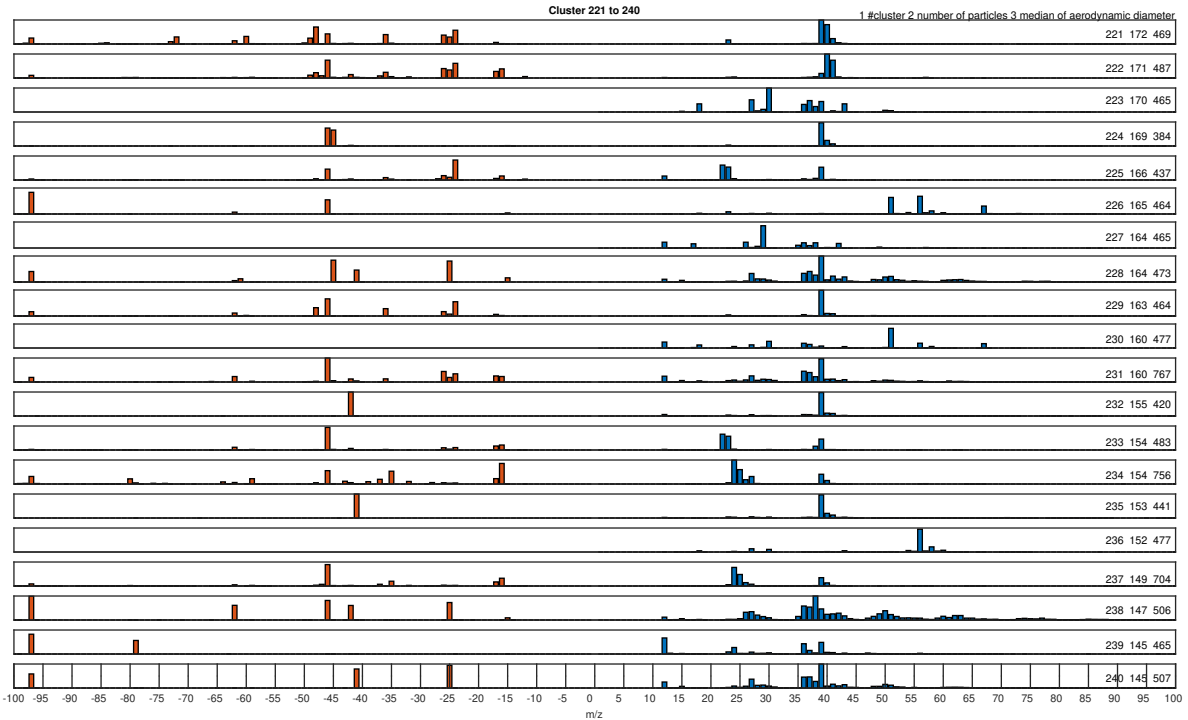
Cluster 221 to 240
1 #cluster 2 number of particles 3 median of aerodynamic diameter
221 172 469
222 171 487
223 170 465
224 169 384
225 166 437
226 165 464
227 164 465
228 164 473
229 163 464
230 160 477
231 160 767
232 155 420
233 154 483
234 154 756
235 153 441
236 152 477
237 149 704
238 147 506
239 145 465
240 145 507
-100 -95 -90 -85 -80 -75 -70 -65 -60 -55 -50 -45 -40 -35 -30 -25 -20 -15 -10 -5 0 5 10 15 20 25 30 35 40 45 50 55 60 65 70 75 80 85 90 95 100
m/z

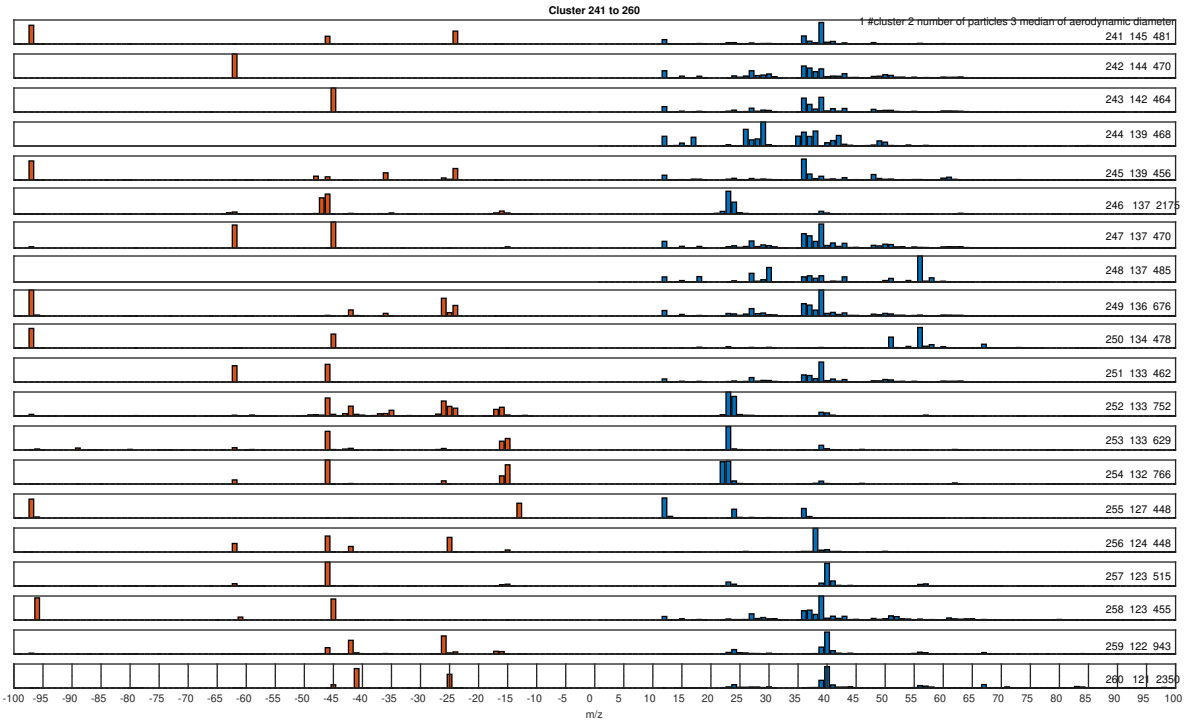
Cluster 241 to 260
1 #cluster 2 number of particles 3 median of aerodynamic diameter
241 145 481
242 144 470
243 142 464
244 139 468
245 139 456
246 137 2175
247 137 470
248 137 485
249 136 676
250 134 478
251 133 462
252 133 752
253 133 629
254 132 766
255 127 448
256 124 448
257 123 515
258 123 455
259 122 943
260 121 2350
-100 -95 -90 -85 -80 -75 -70 -65 -60 -55 -50 -45 -40 -35 -30 -25 -20 -15 -10 -5 0 5 10 15 20 25 30 35 40 45 50 55 60 65 70 75 80 85 90 95 100
m/z

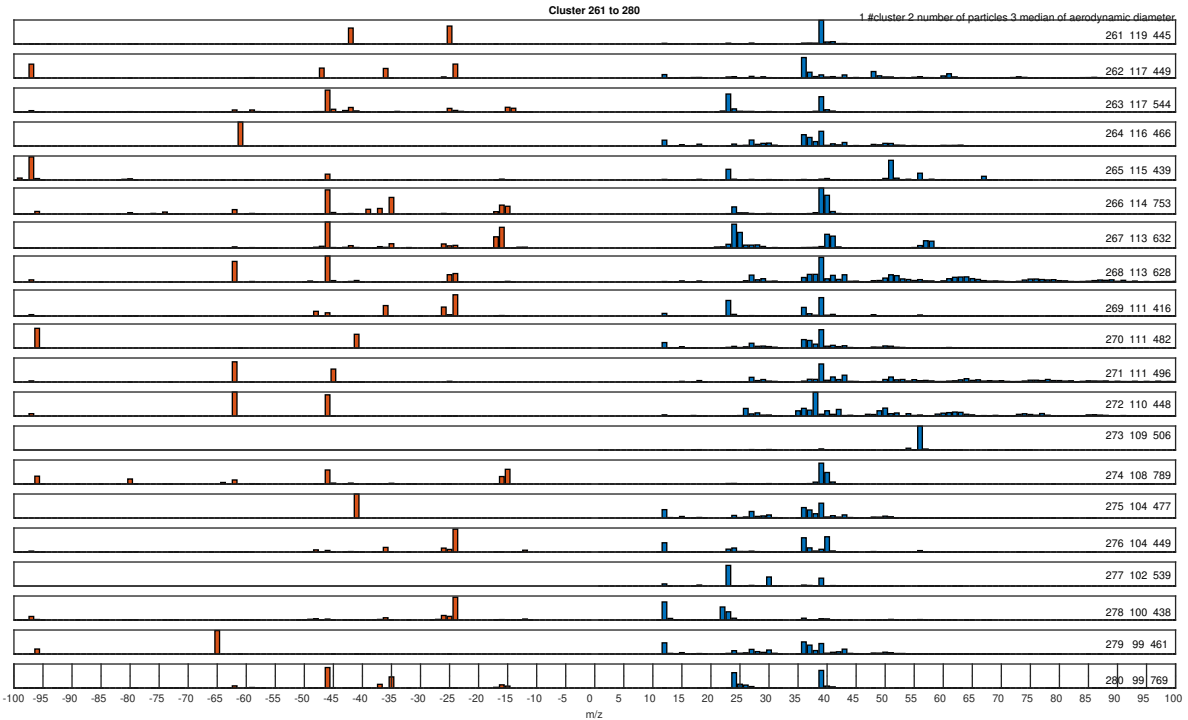
Cluster 261 to 280
1 #cluster 2 number of particles 3 median of aerodynamic diameter
261 119 445
262 117 449
263 117 544
264 116 466
265 115 439
266 114 753
267 113 632
268 113 628
269 111 416
270 111 482
271 111 496
272 110 448
273 109 506
274 108 789
275 104 477
276 104 449
277 102 539
278 100 438
279 99 461
280 99 769
-100 -95 -90 -85 -80 -75 -70 -65 -60 -55 -50 -45 -40 -35 -30 -25 -20 -15 -10 -5 0 5 10 15 20 25 30 35 40 45 50 55 60 65 70 75 80 85 90 95 100
m/z

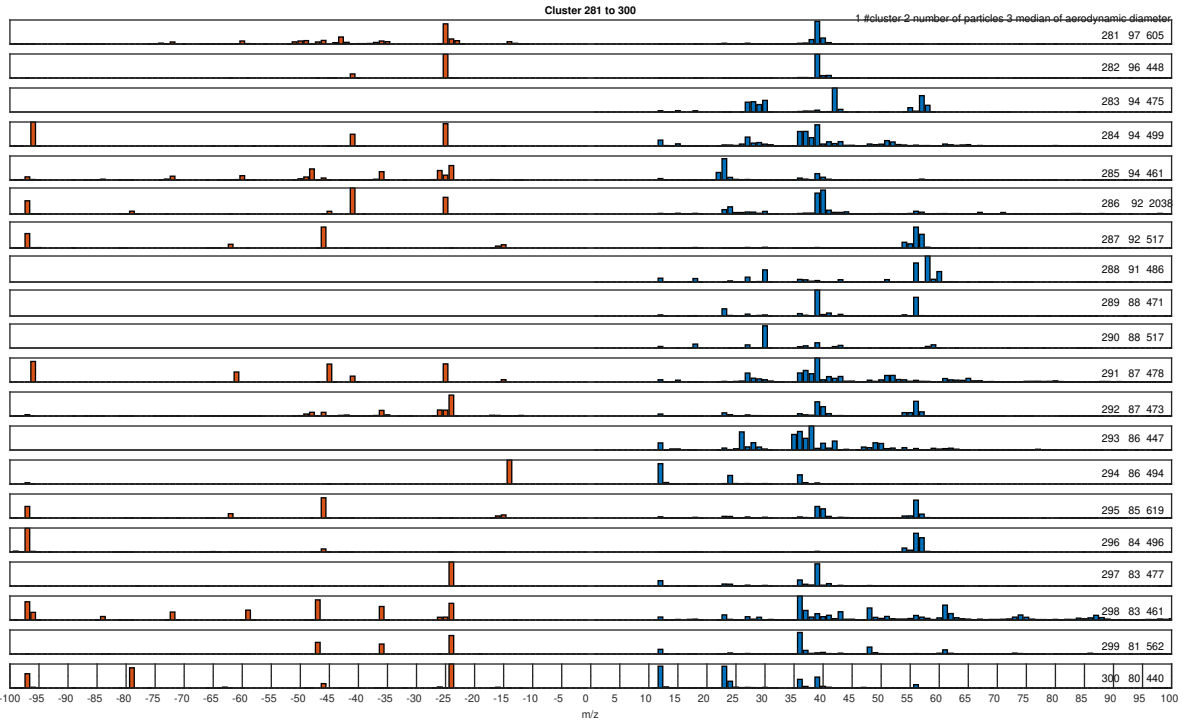
Cluster 281 to 300
1 #cluster 2 number of particles 3 median of aerodynamic diameter
281 97 605
282 96 448
283 94 475
284 94 499
285 94 461
286 92 2038
287 92 517
288 91 486
289 88 471
290 88 517
291 87 478
292 87 473
293 86 447
294 86 494
295 85 619
296 84 496
297 83 477
298 83 461
299 81 562
300 80 440
-100 -95 -90 -85 -80 -75 -70 -65 -60 -55 -50 -45 -40 -35 -30 -25 -20 -15 -10 -5 0 5 10 15 20 25 30 35 40 45 50 55 60 65 70 75 80 85 90 95 100
m/z

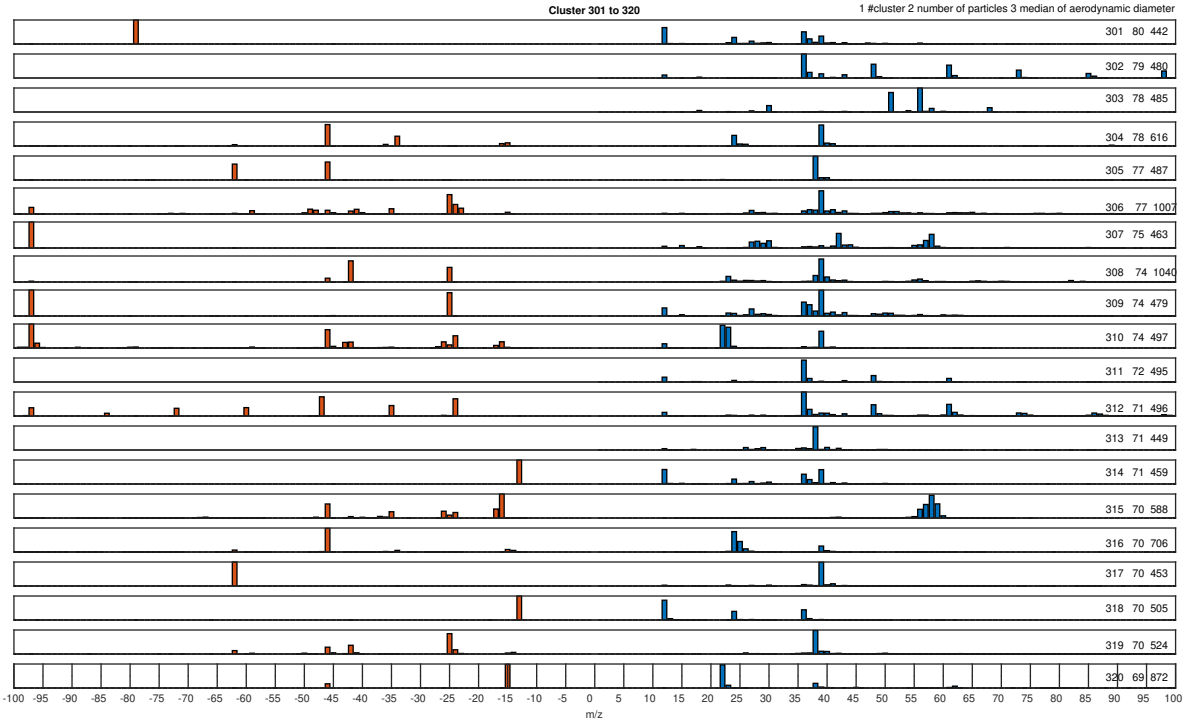
Cluster 301 to 320
1 #cluster 2 number of particles 3 median of aerodynamic diameter
301 80 442
302 79 480
303 78 485
304 78 616
305 77 487
306 77 1007
307 75 463
308 74 1040
309 74 479
310 74 497
311 72 495
312 71 496
313 71 449
314 71 459
315 70 588
316 70 706
317 70 453
318 70 505
319 70 524
320 69 872
-100 -95 -90 -85 -80 -75 -70 -65 -60 -55 -50 -45 -40 -35 -30 -25 -20 -15 -10 -5 0 5 10 15 20 25 30 35 40 45 50 55 60 65 70 75 80 85 90 95 100
m/z

Figure S5: Time series of the top 300 clusters from the ART-2a analysis.

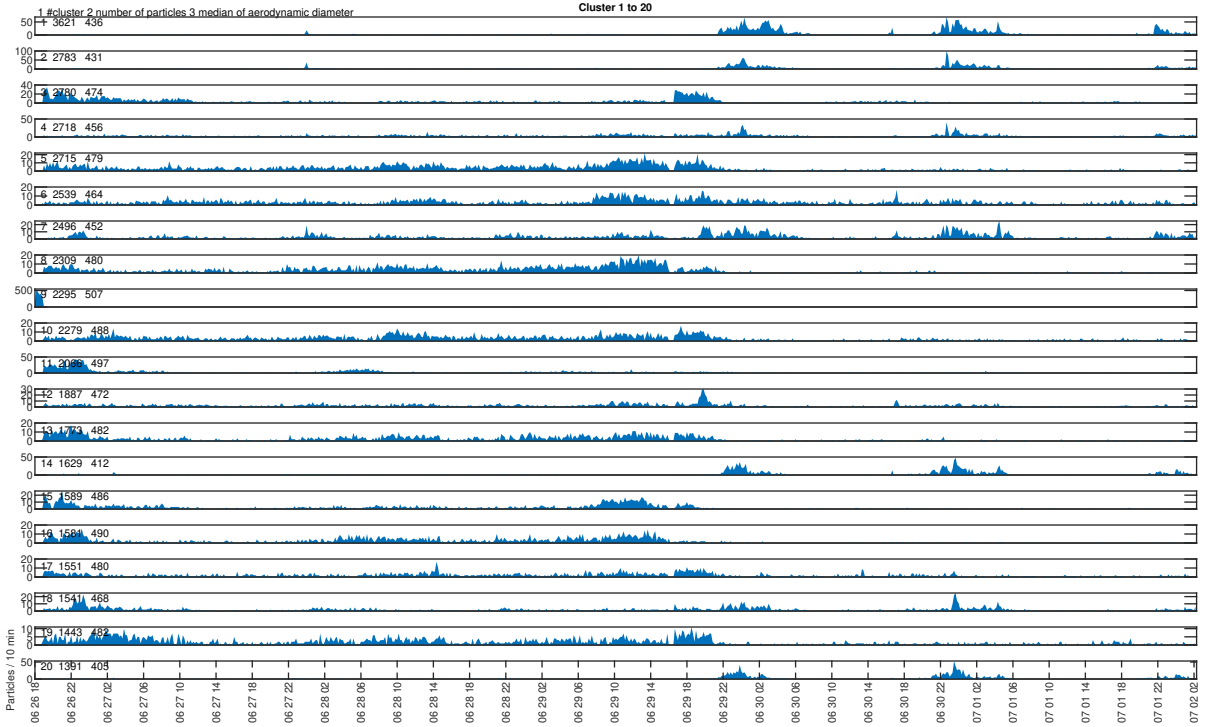

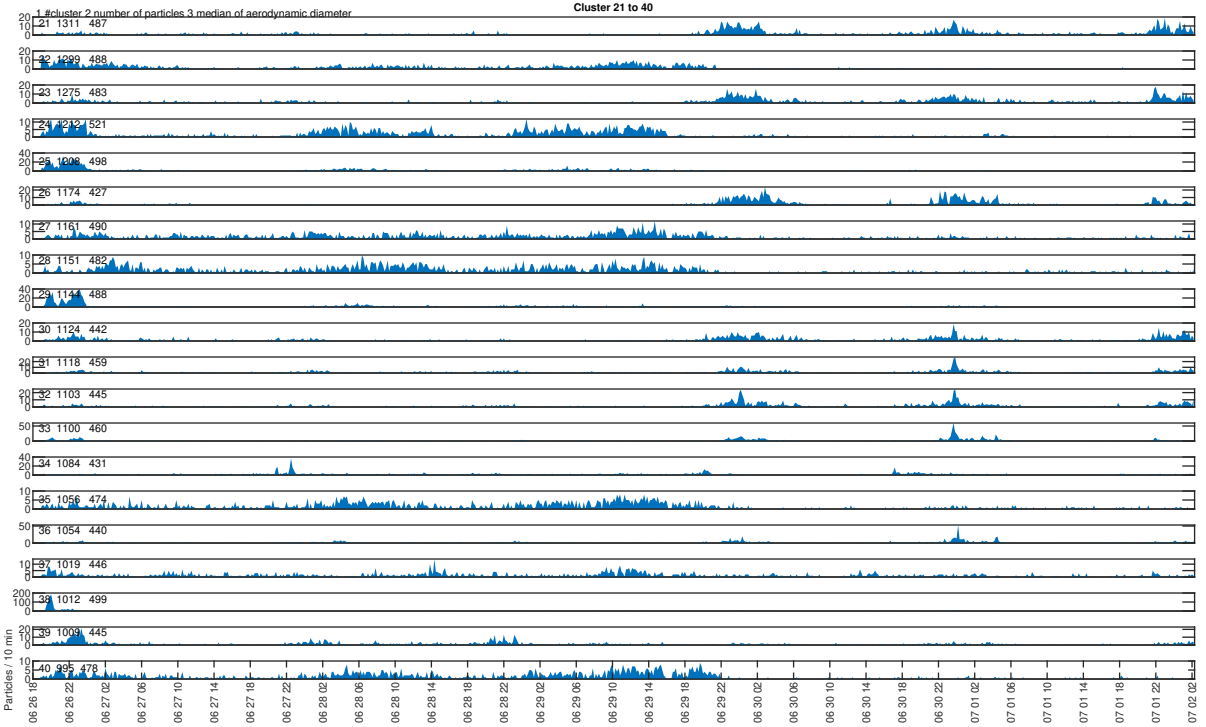
Cluster 21 to 40
1 #cluster 2 number of particles 3 median of aerodynamic diameter
21 1311 487
22 1299 488
23 1275 483
24 1212 521
25 1208 498
26 1174 427
27 1161 490
28 1151 482
29 1144 488
30 1124 442
31 1118 459
32 1103 445
33 1100 460
34 1084 431
35 1056 474
36 1054 440
37 1019 446
38 1012 499
39 1009 445
40 995 478
Particles / 10 min
06 26 18
06 26 22
06 27 02
06 27 06
06 27 10
06 27 14
06 27 18
06 27 22
06 28 02
06 28 06
06 28 10
06 28 14
06 28 18
06 28 22
06 29 02
06 29 06
06 29 10
06 29 14
06 29 18
06 29 22
06 30 02
06 30 06
06 30 10
06 30 14
06 30 18
06 30 22
07 01 02
07 01 06
07 01 10
07 01 14
07 01 18
07 01 22
07 02 02
2018 Local Time (UTC+2h, MM DD HH)

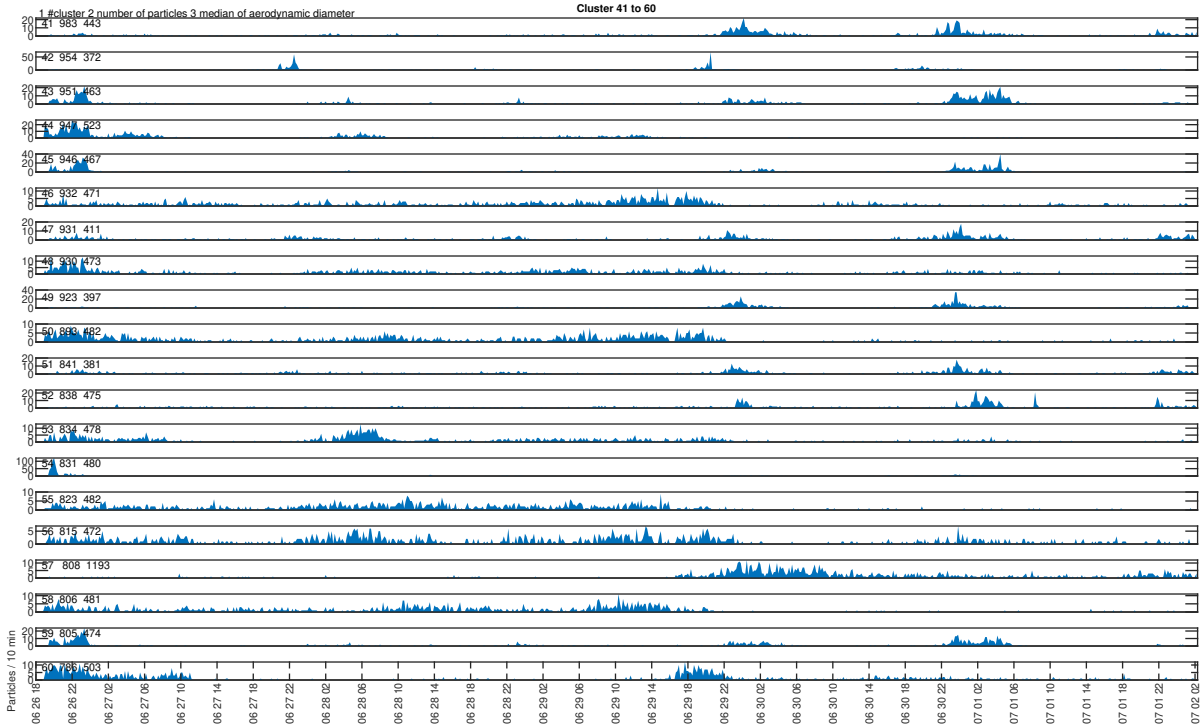
Cluster 41 to 60
1 #cluster 2 number of particles 3 median of aerodynamic diameter
41 983 443
42 954 372
43 951 463
44 944 523
45 946 467
46 932 471
47 931 411
48 930 473
49 923 397
50 889 482
51 841 381
52 838 475
53 834 478
54 831 480
55 823 482
56 815 472
57 808 1193
58 806 481
59 805 474
60 785 503
Particles / 10 min
06 26 18
06 26 22
06 27 02
06 27 06
06 27 10
06 27 14
06 27 18
06 27 22
06 28 02
06 28 06
06 28 10
06 28 14
06 28 18
06 28 22
06 29 02
06 29 06
06 29 10
06 29 14
06 29 18
06 29 22
06 30 02
06 30 06
06 30 10
06 30 14
06 30 18
06 30 22
07 01 02
07 01 06
07 01 10
07 01 14
07 01 18
07 01 22
07 02 02
2018 Local Time (UTC+2h, MM DD HH)

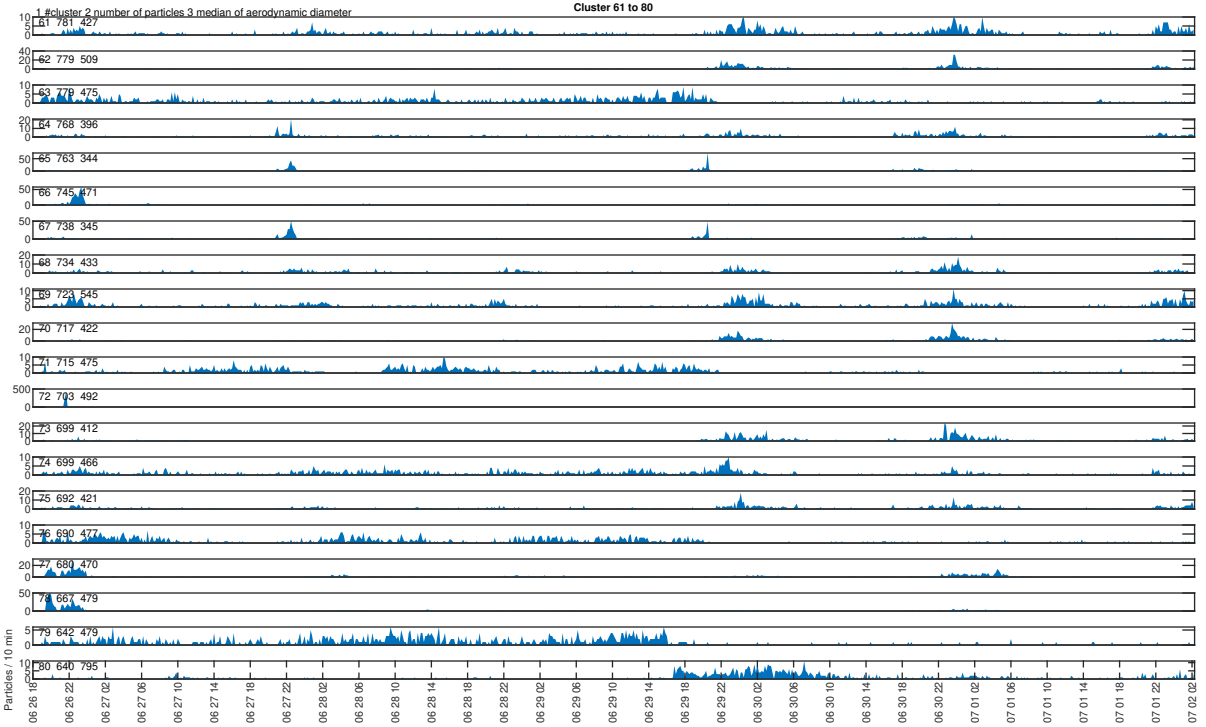
Cluster 61 to 80
1 #cluster 2 number of particles 3 median of aerodynamic diameter
61 781 427
62 779 509
63 778 475
64 768 396
65 763 344
66 745 471
67 738 345
68 734 433
69 723 545
70 717 422
71 715 475
72 703 492
73 699 412
74 699 466
75 692 421
76 690 477
77 680 470
78 667 479
79 642 479
80 640 795
Particles / 10 min
06 26 18
06 26 22
06 27 02
06 27 06
06 27 10
06 27 14
06 27 18
06 27 22
06 28 02
06 28 06
06 28 10
06 28 14
06 28 18
06 28 22
06 29 02
06 29 06
06 29 10
06 29 14
06 29 18
06 29 22
06 30 02
06 30 06
06 30 10
06 30 14
06 30 18
06 30 22
07 01 02
07 01 06
07 01 10
07 01 14
07 01 18
07 01 22
07 02 02
2018 Local Time (UTC+2h, MM DD HH)

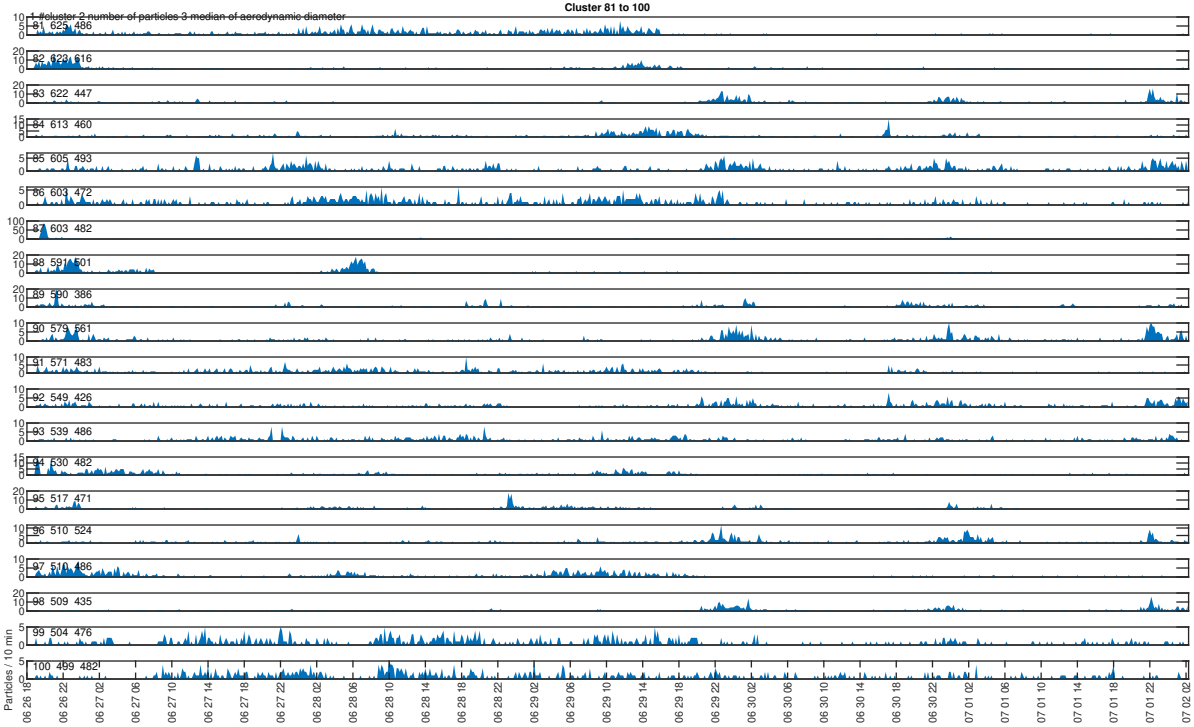
Cluster 81 to 100
1 fcluster 2 number of particles 3 median of aerodynamic diameter
81 625 486
82 623 616
83 622 447
84 613 460
85 605 493
86 603 472
87 603 482
88 591 501
89 590 386
90 579 561
91 571 483
92 549 426
93 539 486
94 530 482
95 517 471
96 510 524
97 510 486
98 509 435
99 504 476
100 499 482
Particles / 10 min
06 26 18
06 26 22
06 27 02
06 27 06
06 27 10
06 27 14
06 27 18
06 27 22
06 28 02
06 28 06
06 28 10
06 28 14
06 28 18
06 28 22
06 29 02
06 29 06
06 29 10
06 29 14
06 29 18
06 29 22
06 30 02
06 30 06
06 30 10
06 30 14
06 30 18
06 30 22
07 01 02
07 01 06
07 01 10
07 01 14
07 01 18
07 01 22
07 02 02
2018 Local Time (UTC+2h, MM DD HH)

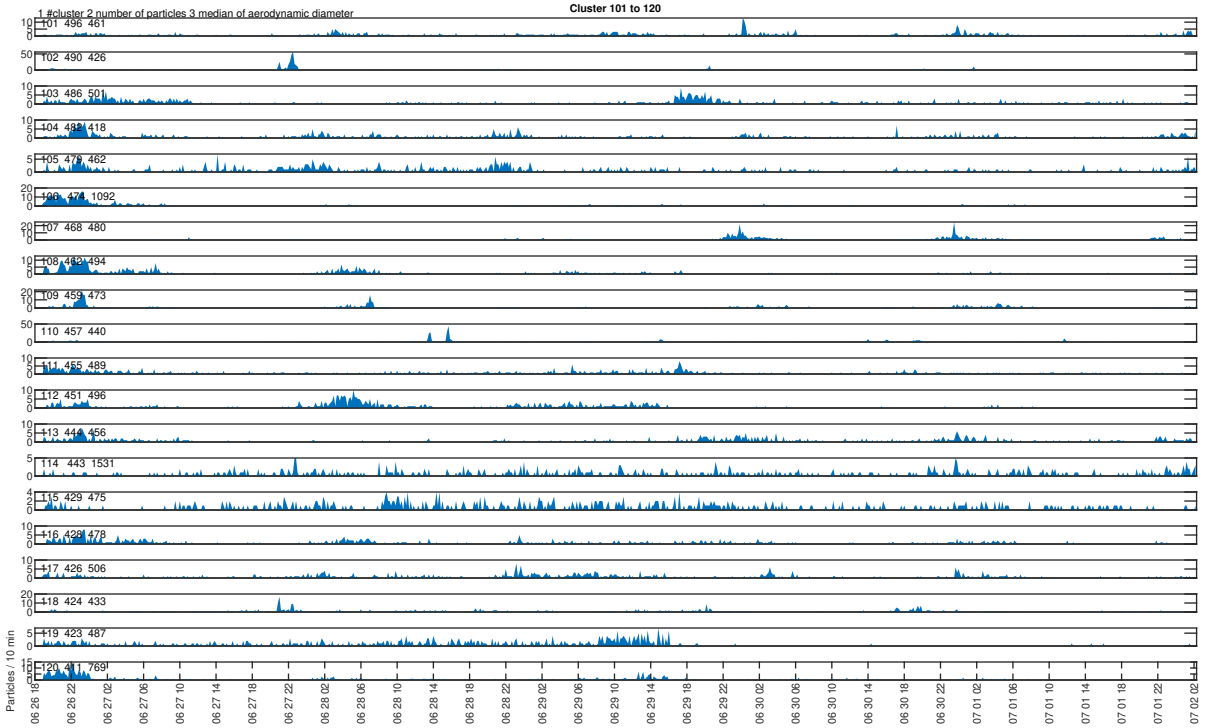
Cluster 101 to 120
1 #cluster 2 number of particles 3 median of aerodynamic diameter
101 496 461
102 490 426
103 486 501
104 482 418
105 479 462
106 474 1092
107 468 480
108 462 494
109 459 473
110 457 440
111 455 489
112 451 496
113 444 456
114 443 1531
115 429 475
116 428 478
117 426 506
118 424 433
119 423 487
120 411 769
Particles / 10 min
2018 Local Time (UTC+2h, MM DD HH)

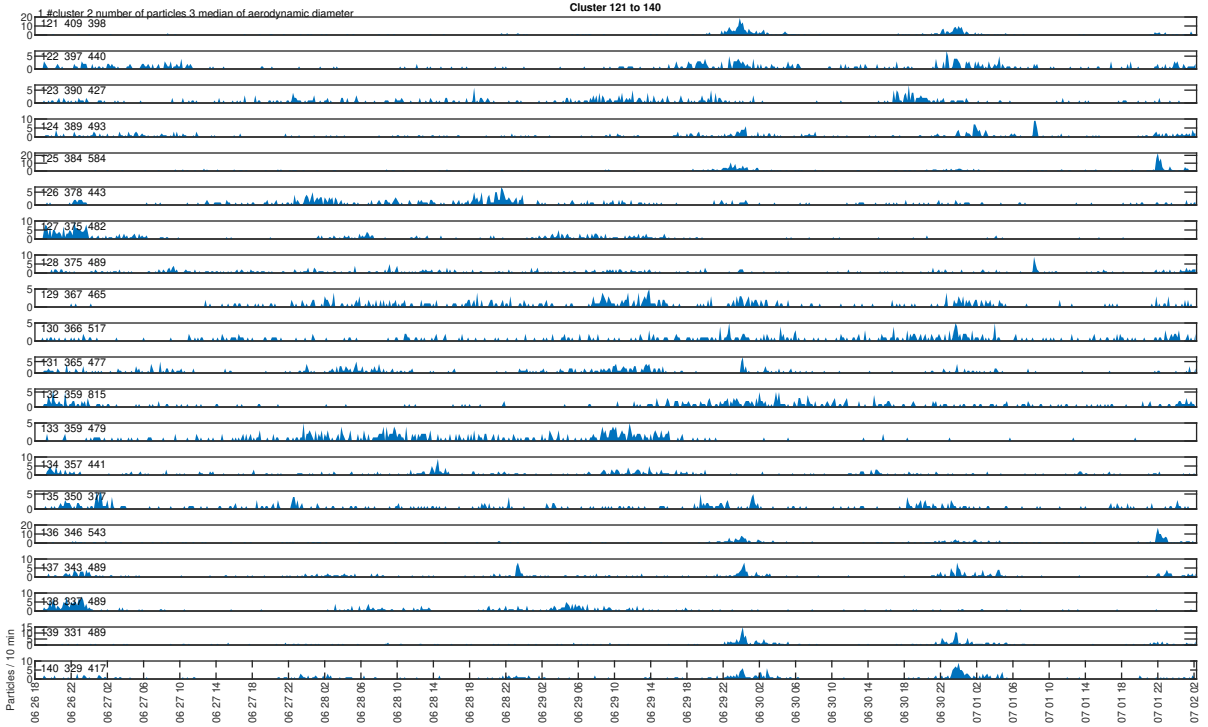
Cluster 121 to 140
1 #cluster 2 number of particles 3 median of aerodynamic diameter
121 409 398
122 397 440
123 390 427
124 389 493
125 384 584
126 378 443
127 375 482
128 375 489
129 367 465
130 366 517
131 365 477
132 359 815
133 359 479
134 357 441
135 350 397
136 346 543
137 343 489
138 337 489
139 331 489
140 329 417
Particles / 10 min
06 26 18
06 26 22
06 27 02
06 27 06
06 27 10
06 27 14
06 27 18
06 27 22
06 28 02
06 28 06
06 28 10
06 28 14
06 28 18
06 28 22
06 29 02
06 29 06
06 29 10
06 29 14
06 29 18
06 29 22
06 30 02
06 30 06
06 30 10
06 30 14
06 30 18
06 30 22
07 01 02
07 01 06
07 01 10
07 01 14
07 01 18
07 01 22
07 02 02
2018 Local Time (UTC+2h, MM DD HH)

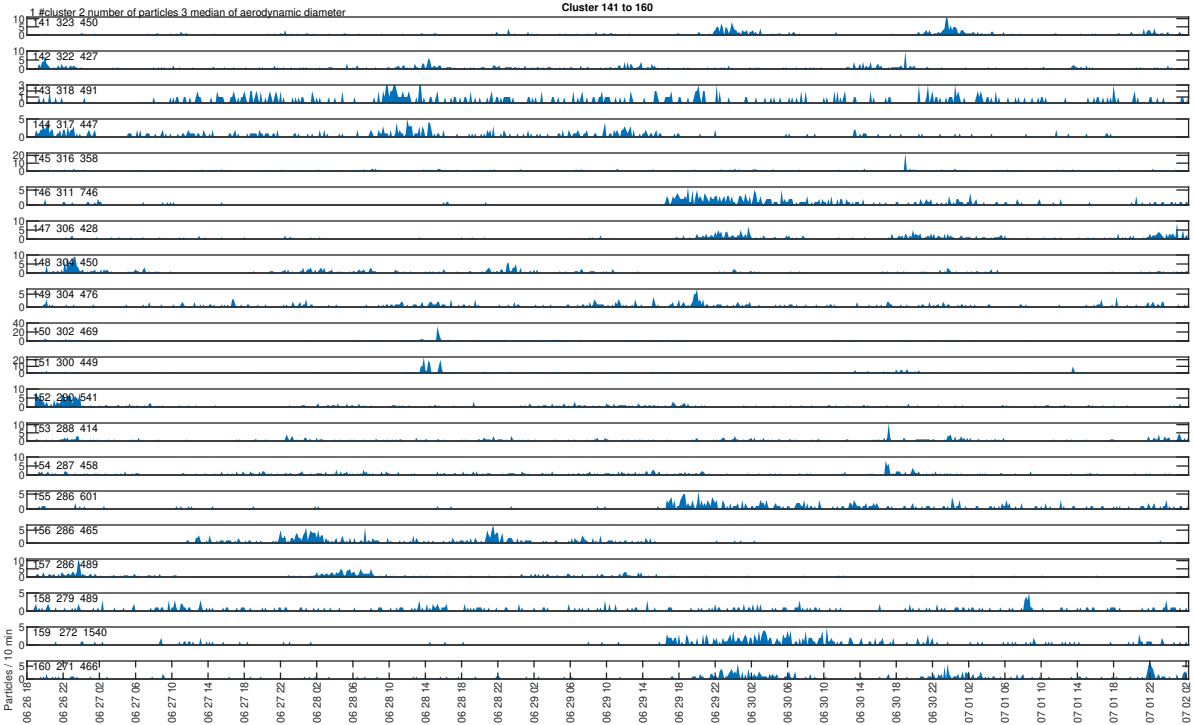
Cluster 141 to 160
1 #cluster 2 number of particles 3 median of aerodynamic diameter
141 323 450
142 322 427
143 318 491
144 317 447
145 316 358
146 311 746
147 306 428
148 304 450
149 304 476
150 302 469
151 300 449
152 290 541
153 288 414
154 287 458
155 286 601
156 286 465
157 286 489
158 279 489
159 272 1540
160 271 466
Particles / 10 min
06 26 18
06 26 22
06 27 02
06 27 06
06 27 10
06 27 14
06 27 18
06 27 22
06 28 02
06 28 06
06 28 10
06 28 14
06 28 18
06 28 22
06 29 02
06 29 06
06 29 10
06 29 14
06 29 18
06 29 22
06 30 02
06 30 06
06 30 10
06 30 14
06 30 18
06 30 22
07 01 02
07 01 06
07 01 10
07 01 14
07 01 18
07 01 22
07 02 02
2018 Local Time (UTC+2h, MM DD HH)

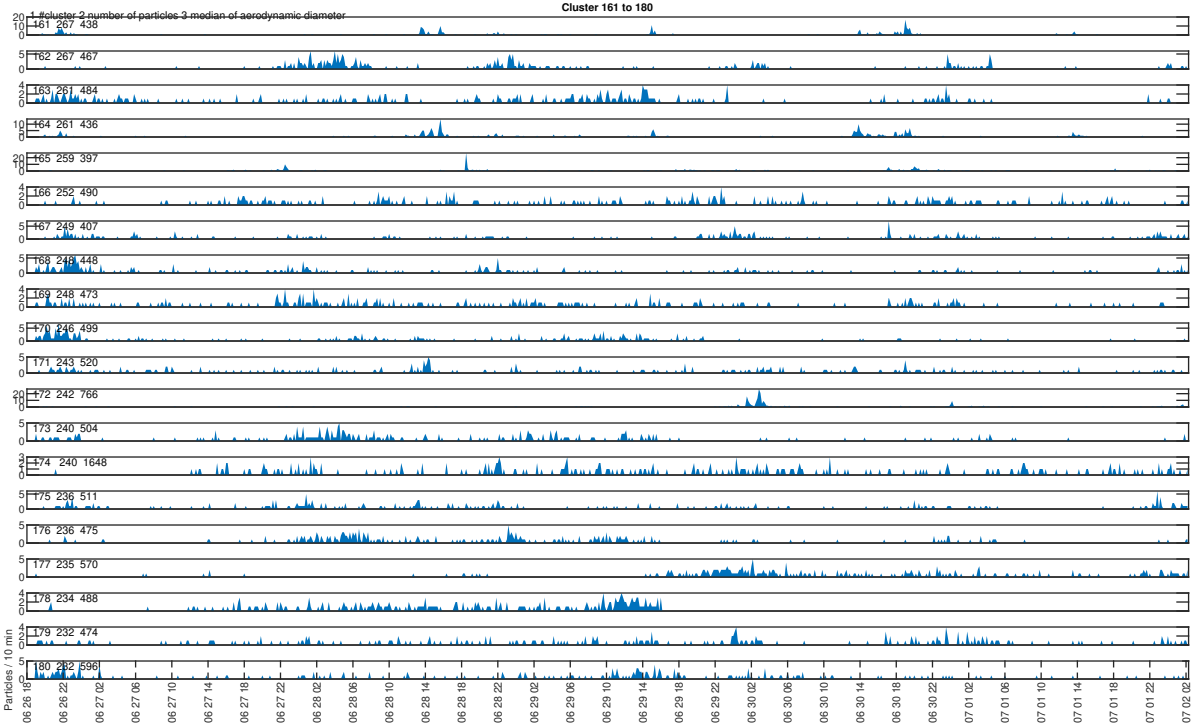
Cluster 161 to 180
1 #cluster 2 number of particles 3 median of aerodynamic diameter
161 267 438
162 267 467
163 261 484
164 261 436
165 259 397
166 252 490
167 249 407
168 248 448
169 248 473
170 246 499
171 243 520
172 242 766
173 240 504
174 240 1648
175 236 511
176 236 475
177 235 570
178 234 488
179 232 474
180 232 596
Particles / 10 min
06 26 18
06 26 22
06 27 02
06 27 06
06 27 10
06 27 14
06 27 18
06 27 22
06 28 02
06 28 06
06 28 10
06 28 14
06 28 18
06 28 22
06 29 02
06 29 06
06 29 10
06 29 14
06 29 18
06 29 22
06 30 02
06 30 06
06 30 10
06 30 14
06 30 18
06 30 22
07 01 02
07 01 06
07 01 10
07 01 14
07 01 18
07 01 22
07 02 02
2018 Local Time (UTC+2h, MM DD HH)

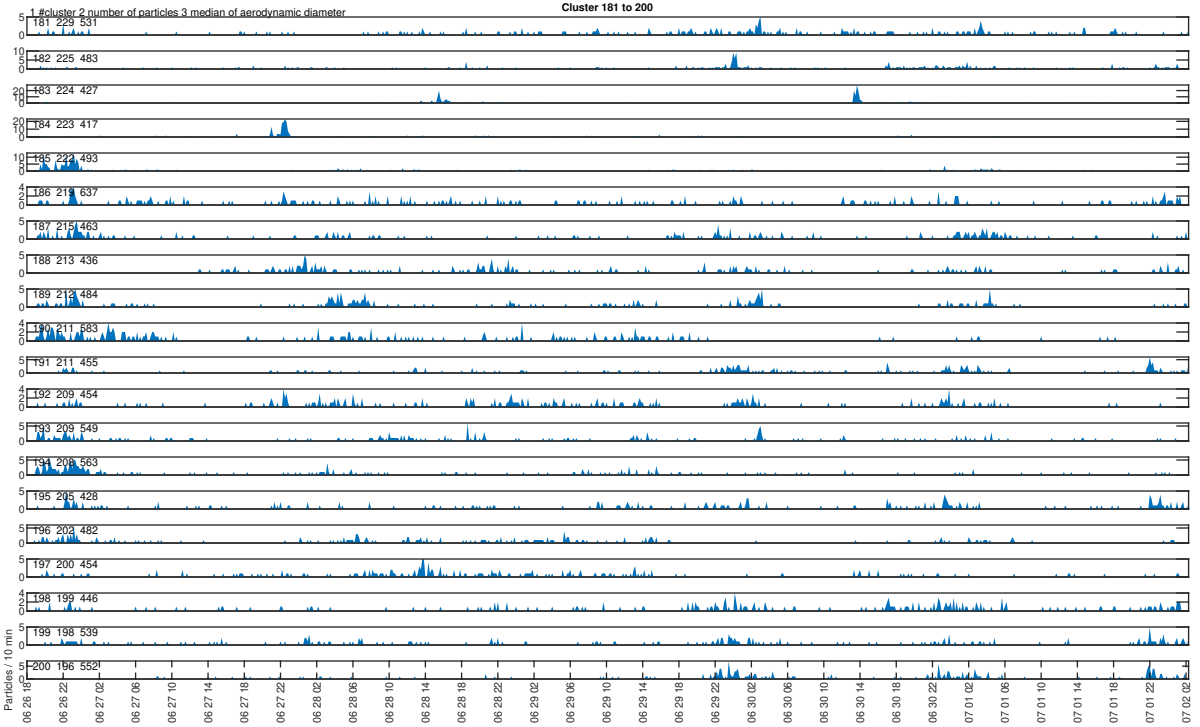
Cluster 181 to 200
1 #cluster 2 number of particles 3 median of aerodynamic diameter
181 229 531
182 225 483
183 224 427
184 223 417
185 222 493
186 219 637
187 215 463
188 213 436
189 212 484
190 211 583
191 211 455
192 209 454
193 209 549
194 208 563
195 205 428
196 202 482
197 200 454
198 199 446
199 198 539
200 196 552
Particles / 10 min
06 26 18
06 26 22
06 27 02
06 27 06
06 27 10
06 27 14
06 27 18
06 27 22
06 28 02
06 28 06
06 28 10
06 28 14
06 28 18
06 28 22
06 29 02
06 29 06
06 29 10
06 29 14
06 29 18
06 29 22
06 30 02
06 30 06
06 30 10
06 30 14
06 30 18
06 30 22
07 01 02
07 01 06
07 01 10
07 01 14
07 01 18
07 01 22
07 02 02
2018 Local Time (UTC+2h, MM DD HH)

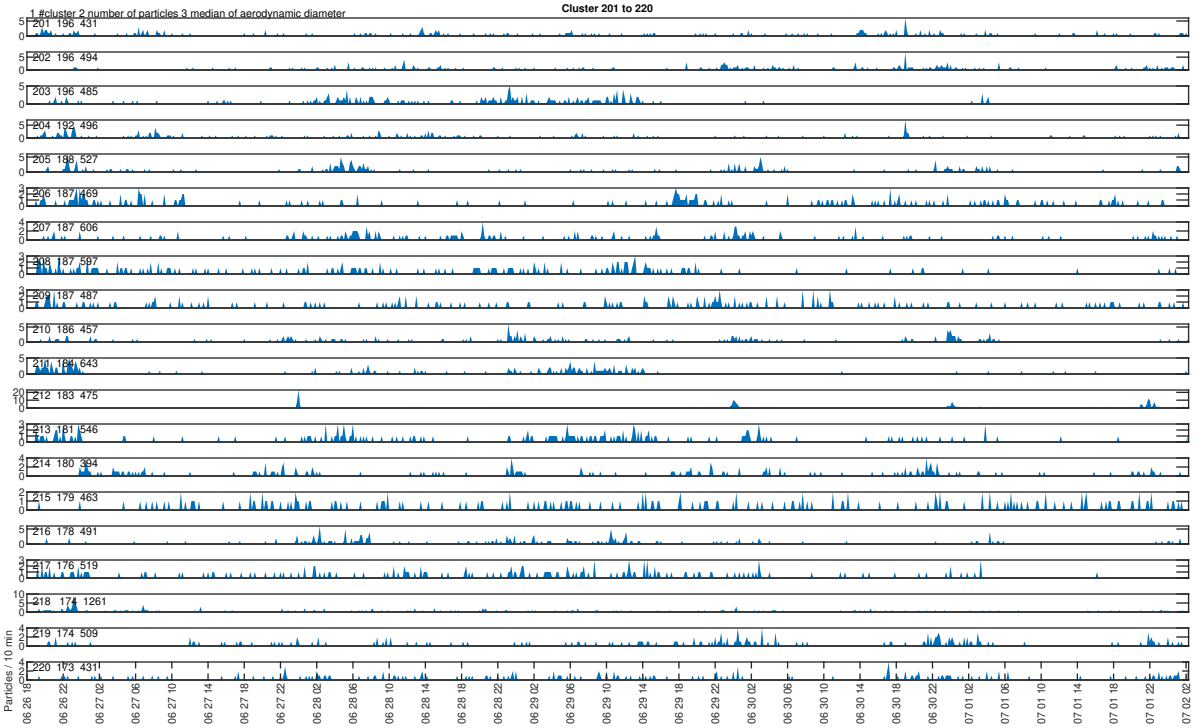
Cluster 201 to 220
1 #cluster 2 number of particles 3 median of aerodynamic diameter
201 196 431
202 196 494
203 196 485
204 192 496
205 188 527
206 187 469
207 187 606
208 187 597
209 187 487
210 186 457
211 186 643
212 183 475
213 181 546
214 180 394
215 179 463
216 178 491
217 176 519
218 174 1261
219 174 509
220 173 431
Particles / 10 min
06 26 18
06 26 22
06 27 02
06 27 06
06 27 10
06 27 14
06 27 18
06 27 22
06 28 02
06 28 06
06 28 10
06 28 14
06 28 18
06 28 22
06 29 02
06 29 06
06 29 10
06 29 14
06 29 18
06 29 22
06 30 02
06 30 06
06 30 10
06 30 14
06 30 18
06 30 22
07 01 02
07 01 06
07 01 10
07 01 14
07 01 18
07 01 22
07 02 02
2018 Local Time (UTC+2h, MM DD HH)

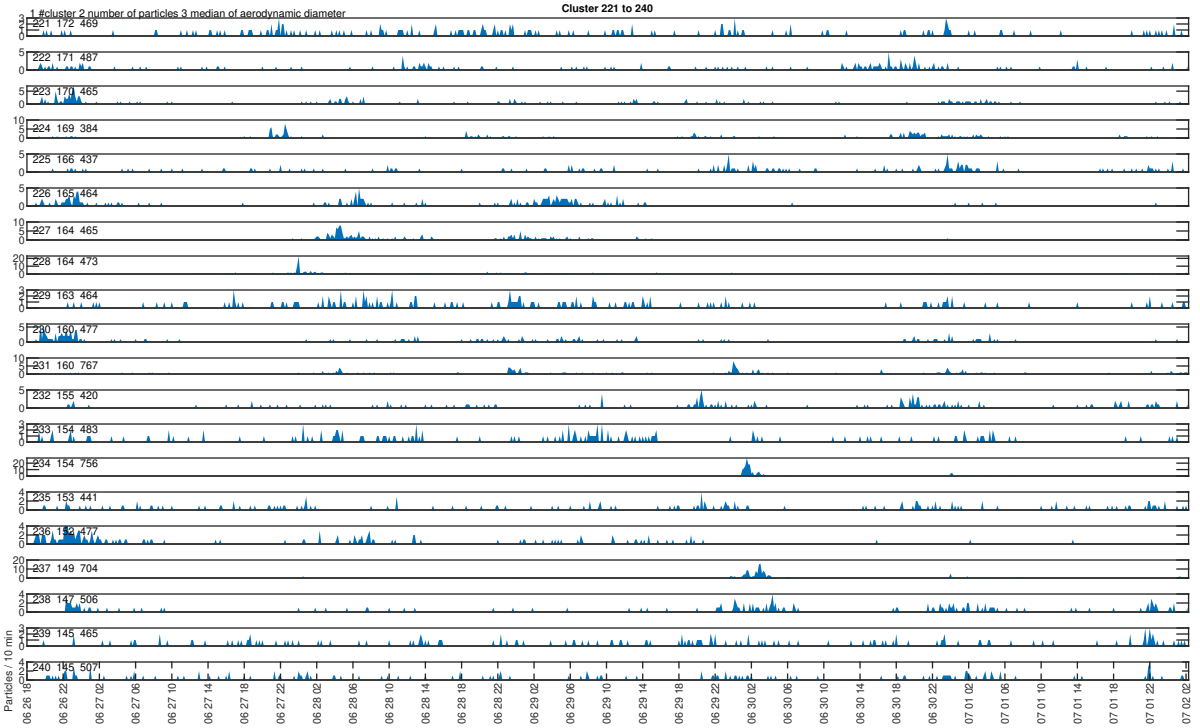
Cluster 221 to 240
1 #cluster 2 number of particles 3 median of aerodynamic diameter
221 172 469
222 171 487
223 170 465
224 169 384
225 166 437
226 165 464
227 164 465
228 164 473
229 163 464
230 160 477
231 160 767
232 155 420
233 154 483
234 154 756
235 153 441
236 152 477
237 149 704
238 147 506
239 145 465
240 145 507
Particles / 10 min
06 26 18
06 26 22
06 27 02
06 27 06
06 27 10
06 27 14
06 27 18
06 27 22
06 28 02
06 28 06
06 28 10
06 28 14
06 28 18
06 28 22
06 29 02
06 29 06
06 29 10
06 29 14
06 29 18
06 29 22
06 30 02
06 30 06
06 30 10
06 30 14
06 30 18
06 30 22
07 01 02
07 01 06
07 01 10
07 01 14
07 01 18
07 01 22
07 02 02
2018 Local Time (UTC+2h, MM DD HH)

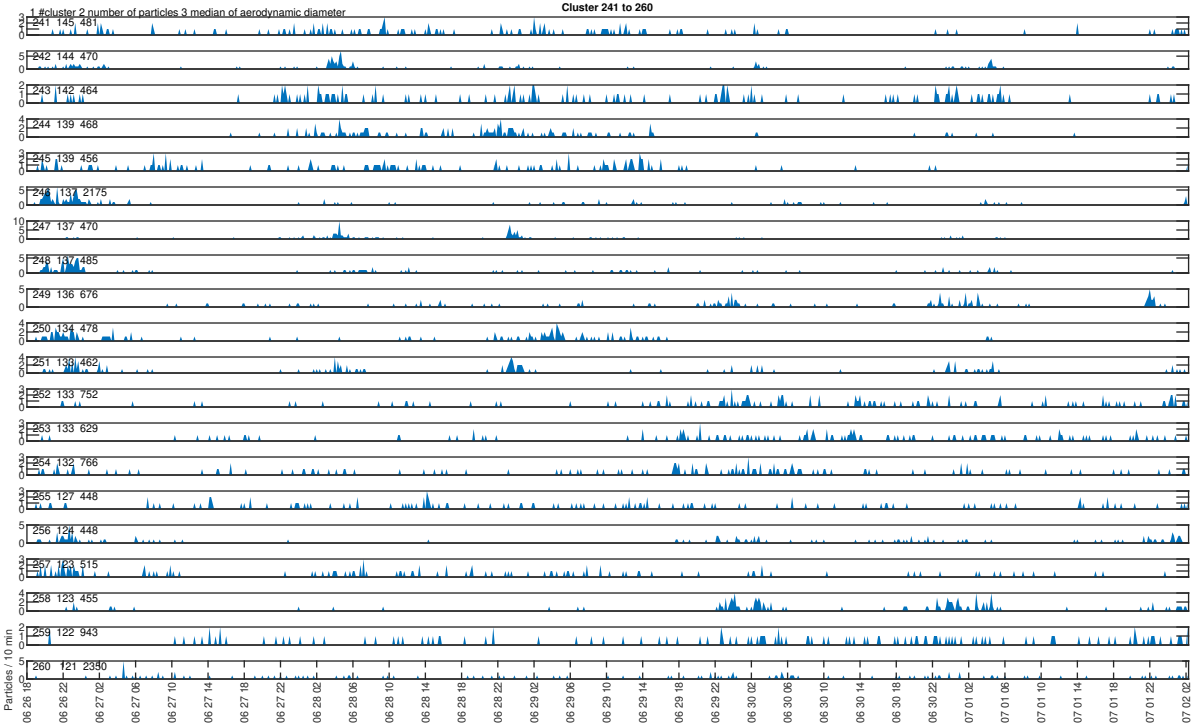
Cluster 241 to 260
1 #cluster 2 number of particles 3 median of aerodynamic diameter
241 145 481
242 144 470
243 142 464
244 139 468
245 139 456
246 137 2175
247 137 470
248 137 485
249 136 676
250 134 478
251 138 462
252 133 752
253 133 629
254 132 766
255 127 448
256 126 448
257 123 515
258 123 455
259 122 943
260 121 2330
Particles / 10 min
06 26 18
06 26 22
06 27 02
06 27 06
06 27 10
06 27 14
06 27 18
06 27 22
06 28 02
06 28 06
06 28 10
06 28 14
06 28 18
06 28 22
06 29 02
06 29 06
06 29 10
06 29 14
06 29 18
06 29 22
06 30 02
06 30 06
06 30 10
06 30 14
06 30 18
06 30 22
07 01 02
07 01 06
07 01 10
07 01 14
07 01 18
07 01 22
07 02 02
2018 Local Time (UTC+2h, MM DD HH)

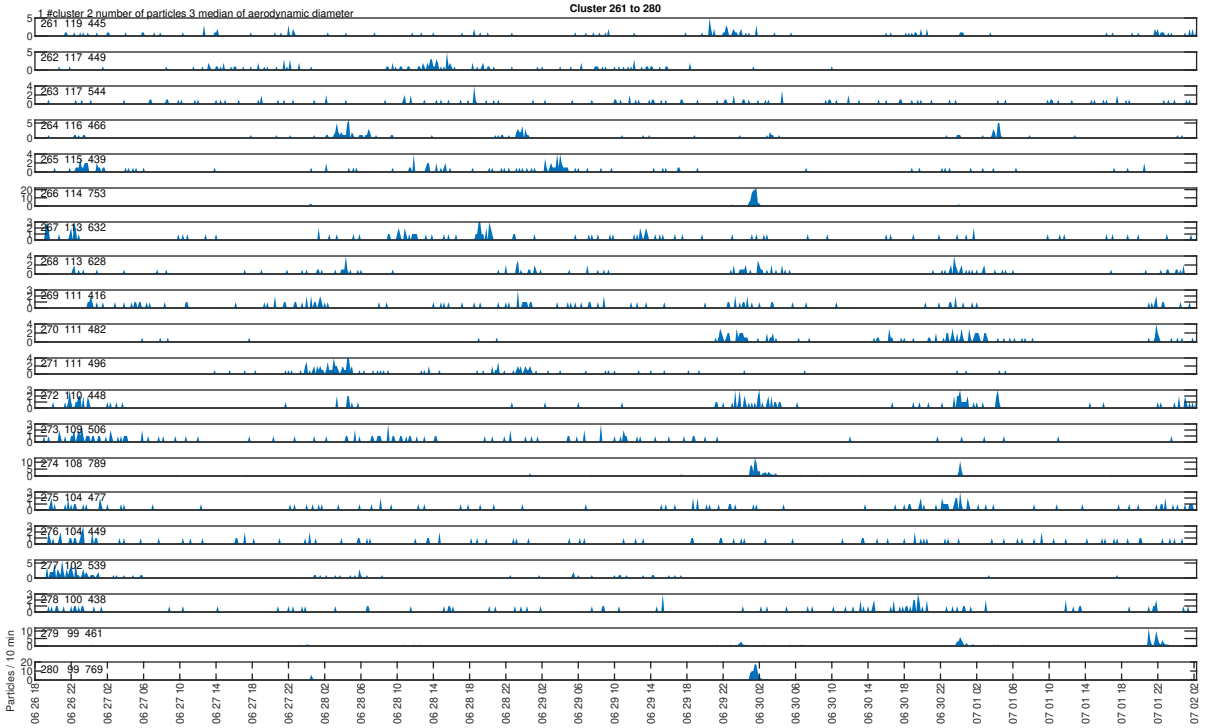
Cluster 261 to 280
1 #cluster 2 number of particles 3 median of aerodynamic diameter
261 119 445
262 117 449
263 117 544
264 116 466
265 115 439
266 114 753
267 113 632
268 113 628
269 111 416
270 111 482
271 111 496
272 110 448
273 109 506
274 108 789
275 104 477
276 104 449
277 102 539
278 100 438
279 99 461
280 99 769
Particles / 10 min
06 26 18
06 26 22
06 27 02
06 27 06
06 27 10
06 27 14
06 27 18
06 27 22
06 28 02
06 28 06
06 28 10
06 28 14
06 28 18
06 28 22
06 29 02
06 29 06
06 29 10
06 29 14
06 29 18
06 29 22
06 30 02
06 30 06
06 30 10
06 30 14
06 30 18
06 30 22
07 01 02
07 01 06
07 01 10
07 01 14
07 01 18
07 01 22
07 02 02
2018 Local Time (UTC+2h, MM DD HH)

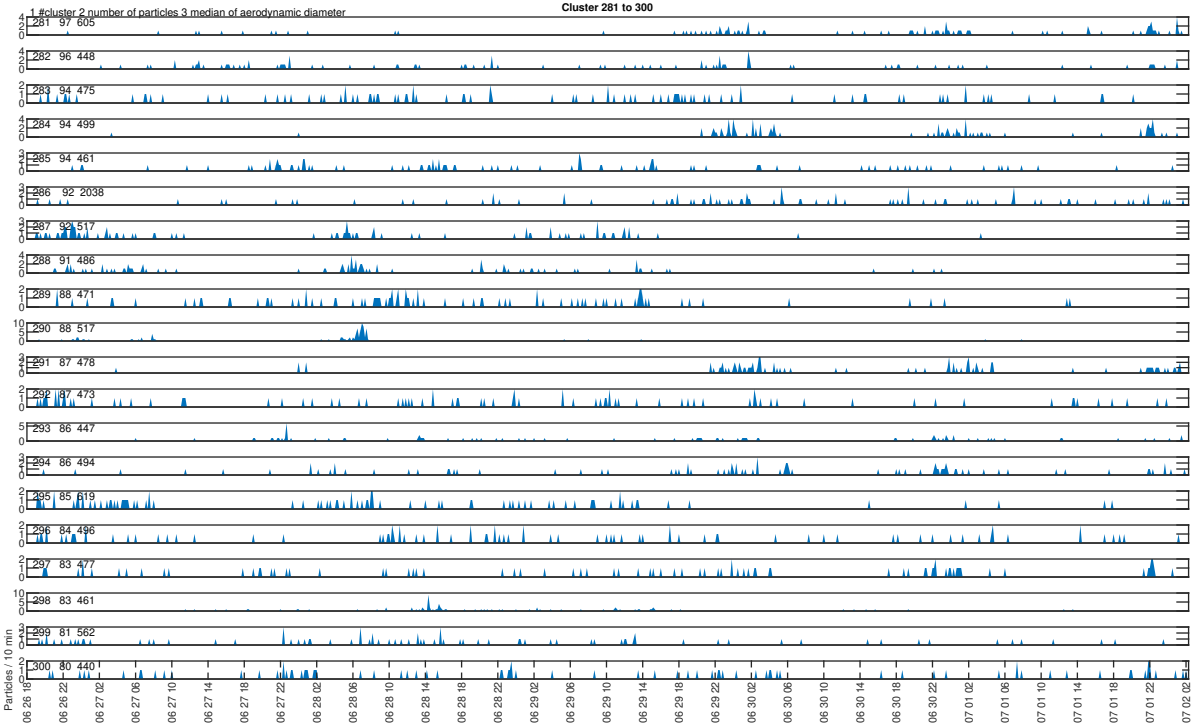
Cluster 281 to 300
1 #cluster 2 number of particles 3 median of aerodynamic diameter
281 97 605
282 96 448
283 94 475
284 94 499
285 94 461
286 92 2038
287 92 517
288 91 486
289 88 471
290 88 517
291 87 478
292 87 473
293 86 447
294 86 494
295 85 619
296 84 496
297 83 477
298 83 461
299 81 562
300 80 440
Particles / 10 min
06 26 18
06 26 22
06 27 02
06 27 06
06 27 10
06 27 14
06 27 18
06 27 22
06 28 02
06 28 06
06 28 10
06 28 14
06 28 18
06 28 22
06 29 02
06 29 06
06 29 10
06 29 14
06 29 18
06 29 22
06 30 02
06 30 06
06 30 10
06 30 14
06 30 18
06 30 22
07 01 02
07 01 06
07 01 10
07 01 14
07 01 18
07 01 22
07 02 02
2018 Local Time (UTC+2h, MM DD HH)

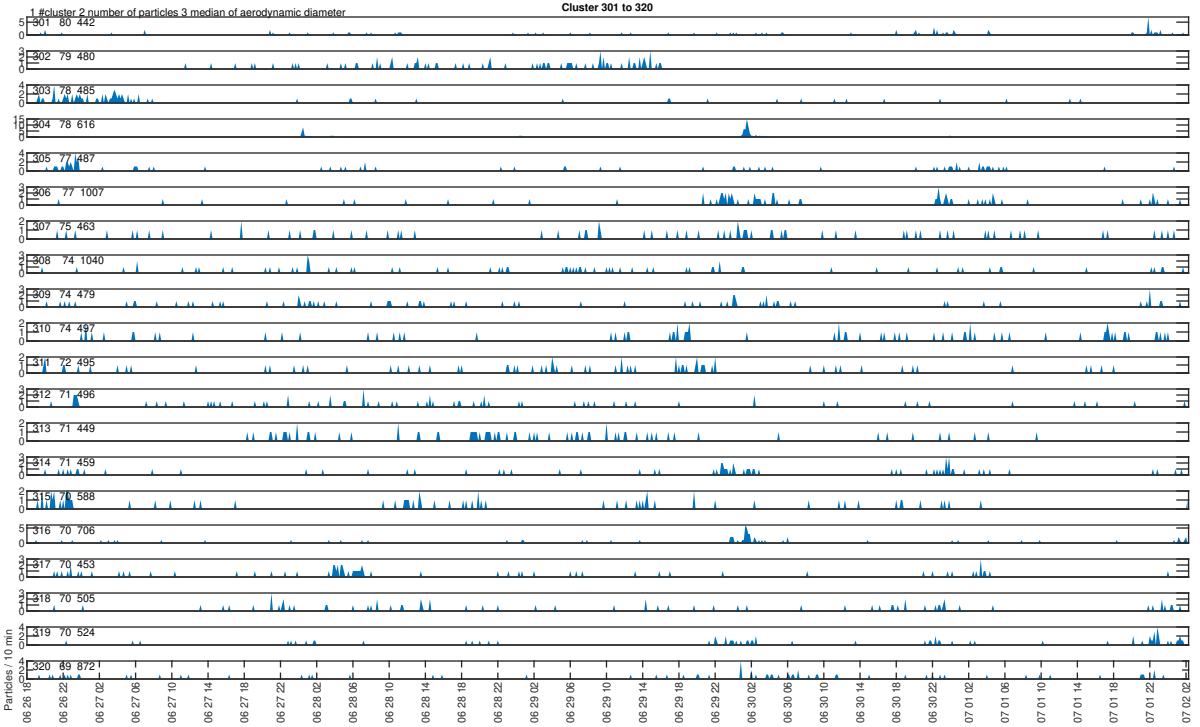
Cluster 301 to 320
1 #cluster 2 number of particles 3 median of aerodynamic diameter
301 80 442
302 79 480
303 78 485
304 78 616
305 77 487
306 77 1007
307 75 463
308 74 1040
309 74 479
310 74 497
311 72 495
312 71 496
313 71 449
314 71 459
315 70 588
316 70 706
317 70 453
318 70 505
319 70 524
320 69 872
Particles / 10 min
06 26 18
06 26 22
06 27 02
06 27 06
06 27 10
06 27 14
06 27 18
06 27 22
06 28 02
06 28 06
06 28 10
06 28 14
06 28 18
06 28 22
06 29 02
06 29 06
06 29 10
06 29 14
06 29 18
06 29 22
06 30 02
06 30 06
06 30 10
06 30 14
06 30 18
06 30 22
07 01 02
07 01 06
07 01 10
07 01 14
07 01 18
07 01 22
07 02 02
2018 Local Time (UTC+2h, MM DD HH)